

1 **Consumer-grade UAV solid-state LiDAR accurately quantifies**
2 **topography in a vegetated fluvial environment**

3
4 Craig John MacDonell^{1*}, Richard David Williams¹, Georgios Maniatis²,
5 Kenny Roberts¹, Mark Naylor³

6 ¹ School of Geographical and Earth Sciences, University of Glasgow,
7 Glasgow, UK

8 ² School of Applied Sciences, University of Brighton, Brighton, UK

9 ³ School of Geosciences, University of Edinburgh, Edinburgh, UK

10 * Correspondence to: Craig MacDonell, School of Geographical and Earth
11 Sciences, University of Glasgow, Glasgow G12 8QQ, UK. E-mail:

12 Craig.MacDonell@glasgow.ac.uk

13
14 **Acknowledgements**

15 Naylor, Williams and MacDonell were funded through NERC grants
16 NE/S003312/1 and NE/T005920/1. RTK-GNSS equipment was provided
17 through NERC Geophysical Equipment Facility Loan 1118. The authors
18 would also like to acknowledge field assistance by Geoffrey Hope-Thomson
19 and also thank Glenfeshie Estate for their ongoing support of our fieldwork.
20 University of Glasgow Sport is thanked for allowing access to the sports
21 field facilities.

22 **Author Contributions (CRediT)**

23 *Conceptualization – R.W., C.M., M.N.; Data curation – C.M., K.R.; Formal*
24 *Analysis – C.M., G.M.; Funding acquisition – M.N., R.W.; Investigation –*
25 *C.M., K.R., R.W.; Methodology – C.M., G.M., K.R.; Software – C.M.;*
26 *Visualization – C.M., G.M.; Writing – original draft – C.M., R.W., G.M.;*
27 *Writing – review & editing – R.W., M.N., C.M., G.M., K.R.*

28 **Pre-print statement**

29 This paper is a non-peer reviewed preprint submitted to EarthArXiv. This
30 paper has been submitted to the Earth Surface Processes and Landforms
31 (ESPL) journal for peer review.

32 **Conflict of interest disclosure**

33 The authors certify that they have no conflict of interest in the subject
34 matter or materials discussed in this manuscript.

36 **Data Availability**

37 Following peer review, the UAV and TLS georeferenced point clouds, GNSS
38 check points and final DEM will be made available from the digital
39 depository at the lead author's institution, with an associated DOI. Prior to
40 completion of peer review, data can be requested by contacting the
41 corresponding author.

37 **1.0 - Introduction**

38 Unoccupied Aerial Vehicles (UAVs; Joyce et al., 2021) have been
39 transformative in providing a platform to deploy sensors to quantify the
40 topography of the Earth's surface, for investigations from the spatial scale
41 of individual landform features upwards (Piégay et al., 2020; Tomsett &
42 Leyland, 2019). Where there are not logistical or legislative constraints to
43 flying, and spatial coverage can be achieved within a day of fieldwork, UAV
44 mounted sensors have largely superseded alternative approaches to
45 surveying, including terrestrial laser scanning (TLS; Brasington et al.,
46 2012; Williams et al., 2014; Alho et al., 2011). Sensors that have been
47 mounted onto UAVs to acquire observations that can be used to
48 subsequently reconstruct topography can be grouped into two remote
49 sensing categories: passive and active (Lillesand et al., 2015). To date, the
50 former category has dominated geomorphological applications but
51 technological developments in LiDAR technology herald the potential for the
52 return of more active remote sensing methods for topographic
53 reconstruction.

54
55 Passive sensors include digital cameras that are used to acquire images
56 that are subsequently used in Structure from Motion (SfM)
57 photogrammetry (Smith et al., 2016). Whilst SfM photogrammetry has
58 enabled a plethora of geomorphic investigations (e.g. Bakker and Lane,
59 2017; Marteau et al., 2017; Cucchiaro et al., 2018; Llena et al., 2020;
60 Eschbach et al., 2021), there are aspects of SfM photogrammetry that limit
61 what can be achieved to reconstruct topography. The passive nature of the
62 technology poses particular problems for reconstruction bare earth
63 topography; imagery cannot penetrate vegetation cover and vegetated
64 areas are typically associated with poorer processing quality due to weaker
65 image matching (Carrivick et al., 2016; Eltner et al., 2016; Iglhaut et al.,
66 2019; Resop et al., 2019). Shadows caused by vegetation and/or
67 topographic features also reduce and sometimes eliminate the
68 effectiveness of SfM photogrammetry in what are often key areas of a
69 survey such as steep river banks that are geomorphologically dynamic
70 (Kasvi et al., 2019; Resop et al., 2019). Whilst workflows to minimise
71 potential systematic errors, such as large forward and lateral overlap of
72 imagery, as well as double grid flying patterns (James & Robson, 2014;
73 Wackrow & Chandler, 2011) have been established these don't overcome
74 localised errors that arise from image quality and in many situations they
75 significantly add to UAV flight time.

76

77 In contrast to SfM photogrammetry, active remote sensing offers direct
78 survey of topography. Airborne Light Detection and Ranging (LiDAR)
79 surveys (Glennie et al., 2013), that have been acquired using sensors
80 mounted on crewed planes or helicopters, have been transformative in
81 enabling the construction of Digital Elevation Models (DEMs) at spatial
82 scales $>1 \text{ km}^2$. Such datasets have been widely used for a variety of
83 geomorphological investigations (Clubb et al., 2017; Jones et al., 2007;
84 Sofia et al., 2014). Whilst the importance of these sensors cannot be
85 understated (Tarolli & Mudd, 2020), the cost of the instruments and
86 associated deployment logistics have limited most geomorphologists to
87 using archival airborne LiDAR datasets (Crosby et al., 2020). Early
88 integration of LiDAR sensors on UAV platforms was demonstrated in
89 forestry applications (Jaakkola et al., 2010; Lin et al., 2011; Wallace et al.,
90 2012). More recently, UAV LiDAR including topographic-bathymetric
91 systems have been demonstrated across several fluvial environments and
92 applications (e.g. Resop et al., 2019; Mandlbürger et al., 2020; Islam et
93 al., 2021; Resop et al., 2021). Despite these pertinent examples, the
94 growth trajectory of UAV LiDAR surveys remains significantly slower than
95 the comparable rate for UAV SfM photogrammetry when it was in its
96 geomorphic application infancy (Babbel et al., 2019; Pereira et al., 2021),
97 due to the relatively high entry cost of LiDAR sensors and associated large
98 payload UAV platforms that are required. However, a new generation of
99 cheaper, solid state LiDAR sensors (Štroner et al., 2021) offers potential
100 for a return to active remote sensing of dry topography, now using UAV
101 platforms. However, this technology has not yet been applied and assessed
102 in geomorphic environments.

103

104 LiDAR measurements in their traditional form consist of a pulse or wave
105 being emitted from a laser sensor, which is steered across an area of
106 interest using moving components (i.e. mirrors) which are precisely aligned
107 and regularly calibrated. Either the time-of-flight between the emission of
108 the laser and its subsequent reflection, or variability in the reflected laser
109 frequency, are then used to determine range. Many LiDAR sensors can also
110 detect multiple returns (Resop et al., 2019; Wallace et al., 2012), usually
111 based on the intensity of the return. In contrast to traditional LiDAR, solid-
112 state LiDAR systems feature few or no moving parts, based on modern
113 electronics. They use an array of aligned sensors, which when combined
114 enable significantly increased scanning rates (Velodyne LiDAR, 2022). The
115 development of solid-state LiDAR can be traced back to obstacle avoidance
116 and navigation for autonomous vehicle development in the mid-2000s
117 when the limited scanning rate of mechanical LiDAR systems was deemed

118 insufficient for these tasks (Pereira et al., 2021; Raj et al., 2020). The
119 difference between mirror-based mechanical and solid-state LiDAR systems
120 parallels the difference between traditional whiskbroom and newer push-
121 broom scanning systems found on space-based satellites (Abbasi-
122 Moghadam & Abolghasemi, 2015). The change in internal components from
123 mechanical to electronic resolves limitations in mounting LiDAR units on
124 UAVs due to the relatively large size, fragility, and the cost of mirror-based
125 sensors. Indeed, the escalating demand for solid-state LiDAR units from
126 automotive, robotic production line and autonomous delivery industries
127 (Kim et al., 2019) has necessitated scalable manufacture of these units and
128 a subsequent reduction in unit cost. Moreover, automotive specifications
129 for this technology have demanded a wide field-of-view (FOV) and fine
130 angular resolution to enable higher detail at longer range, meaning solid-
131 state instruments are often of comparable or better quality than their
132 traditional mechanical counterparts.

133

134 The aim of this paper is to evaluate the performance of a consumer-grade
135 solid state LiDAR sensor mounted on a UAV to reconstruct the topography
136 of a geomorphic environment. Our first objective is to acquire and process
137 LiDAR point clouds using a variety of UAV flight heights and speeds, and
138 assess their associated horizontal and vertical errors, for a test case; a
139 survey of an artificial grass football pitch. Our second objective is to acquire
140 and assess a LiDAR survey of a 3 km long reach of the braided River Feshie
141 to quantify dry topography. Our motivation is to consider whether
142 consumer-grade LiDAR offers advantages to the existing set of geomatics
143 technologies that are available for geomorphologists to quantify the form
144 of the Earth's surface. In the discussion we reflect upon these relative
145 advantages, and we offer recommendations for acquiring airborne LiDAR
146 surveys with UAVs.

147 **2.0 - LiDAR sensor and field setting**

148 We focus upon testing a DJI Zenmuse L1 solid-state LiDAR sensor, which
149 integrates a Livox AVIA solid-state LiDAR module, a high-accuracy Inertial
150 Measurement Unit (IMU), and a camera with a 1-inch CMOS
151 (Complementary Metal Oxide Semiconductor) sensor on a 3-axis stabilized
152 gimbal. The DJI L1 solid-state LiDAR sensor was mounted on a DJI Matrice
153 300 Real-Time Kinematic (RTK) UAV platform, which is capable of
154 undertaking mapping flights of around 35 minutes with the sensor payload.
155 The aircraft and sensor were linked to a D-RTK 2 GNSS base station by
156 radio to enable the receipt of accurate RTK-GNSS position data.

157

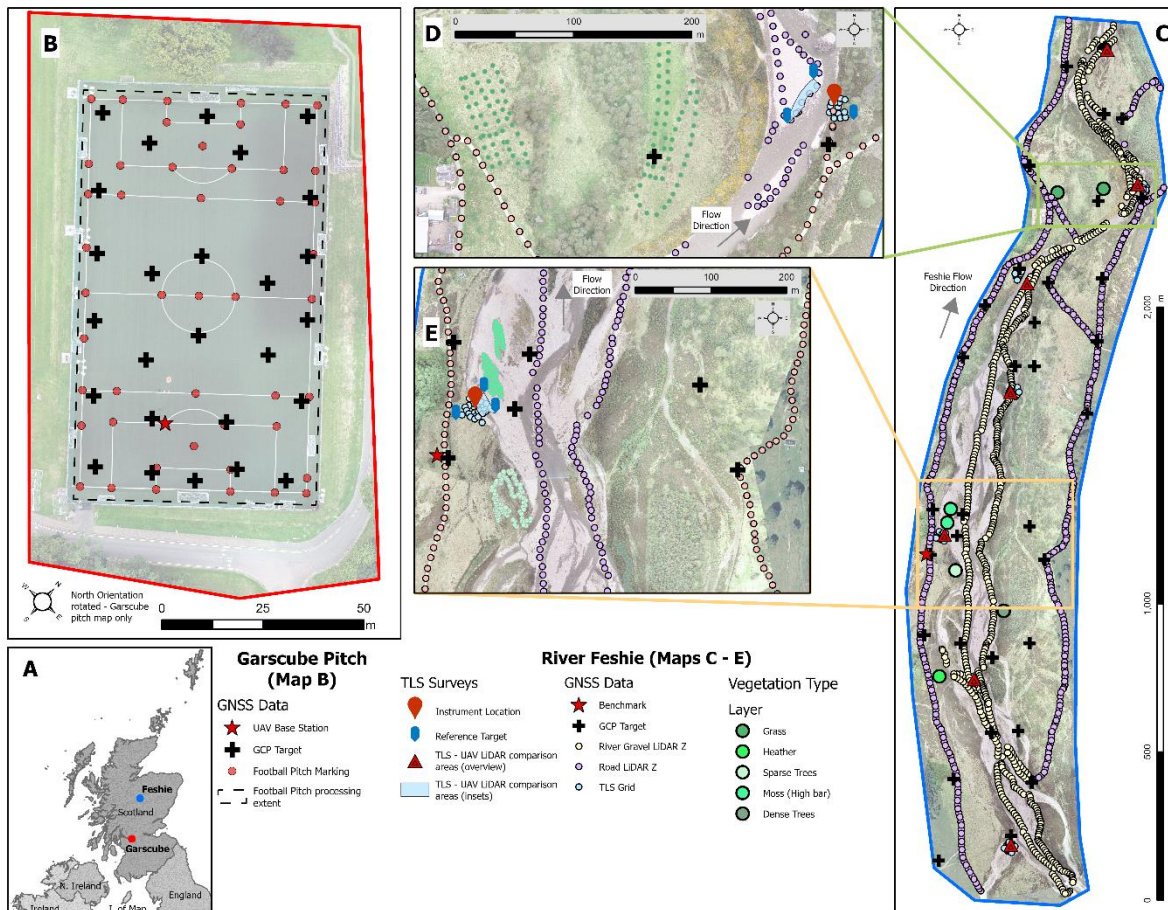
158 Testing of the DJI L1 solid-state LiDAR system was undertaken at the
159 University of Glasgow Garscube Sports Campus (Figure 1b) to assess the
160 positional accuracy of the system. An artificial sport pitch was chosen for
161 the test area, given the relative flatness of the football pitch, the abundance
162 of pitch markings for check points, and the ability to easily distribute and
163 position a further dense grid of ground control targets.

164

165 A braided reach of the River Feshie, Scotland, was chosen to assess the
166 LiDAR system (Figure 1c). This reach is iconic as a site to assess geomatics
167 technologies for the quantification of topography, including RTK-GNSS
168 (Brasington et al., 2000), aerial blimps (Vericat et al., 2008), terrestrial
169 laser scanning (Brasington et al., 2012), wearable LiDAR (Williams et al.,
170 2020a) and RTK-GNSS positioned UAV imagery for SfM photogrammetry
171 (Stott et al., 2020), as well as geomorphological application to quantify
172 sediment budgets (Wheaton et al., 2010), and to shed light on the
173 mechanisms of channel change (Wheaton et al., 2013). This history of
174 innovation, and the low vertical amplitude of topographic variation, made
175 this both an ideal and challenging site to test the use of the LiDAR in a
176 natural environment. The Feshie reach is characterised by a D_{50} surface
177 grain size of 50 to 110 mm (Brasington et al., 2012). At the time of survey,
178 the reach featured a network of shallow anabranches, which were up to c.
179 1 m in depth and occupied ~15% of the active width. The active reach
180 features a number of vegetated bars, colonised with grasses, sedges, and
181 heather, as well as Scots Pine (*Pinus sylvertris*), silver birch (*Betula*
182 *pendula*) and common/grey alder (*Alnus glutinosa/Alnus incana*). Across
183 the River Feshie riverscape, woody vegetation densities are generally
184 increasing across the valley bottom, including within and on the banks of
185 the active channel, due an active and ongoing approach to manage deer
186 numbers (Ballantyne et al., 2021). The presence of a variety of vegetation,
187 with different heights and densities, presents a useful applied context for

188 evaluating the ability of the LiDAR system to detect ground returns through
 189 vegetation canopies and for point cloud processing algorithms to filter
 190 vegetation returns.

191



192

193 Figure 1: Overview of the two study sites, a) showing the location of the
 194 Garscube site near Glasgow and the Feshie site in the Cairngorms
 195 National Park, b) the dense control network across the artificial football
 196 pitch at Garscube site, c) an overall view of the Feshie survey with GNSS
 197 points along roads, river gravel and in vegetation, along with TLS
 198 surveys, d) and e) to zoomed insets showing more detail of the additional
 199 GNSS and TLS surveys.

200 3.0 - Methods

201 3.1 - UAV LiDAR data collection

202 Flights were planned directly in the DJI Pilot app on the aircraft controller,
 203 using imported KML polygon areas. Automated IMU calibration was
 204 activated; LiDAR scan side overlap was set to 50%; and triple returns were
 205 recorded, with a sampling rate of 160 kHz. The flight path pattern was
 206 aligned at both sites to remain within UK CAA Visual Line-of-Sight
 207 recommendations for flying UAVs. Moreover, the flight path patterns
 208 ensured that sufficiently frequent sharp turning (every 100 seconds or

209 every 1000 m with flight speed of 10 m/s) was undertaken for IMU
 210 calibration purposes, in-line with the manufacturer recommendations. The
 211 LiDAR data were stored on an SD card within the DJI L1 solid-state LiDAR
 212 sensor.

213
 214 This initial testing at Garscube consisted of four flights over a synthetic
 215 football pitch and surrounds, each with different flying height and speed
 216 variables (Table 1). At the River Feshie site, the required flight path pattern
 217 resulted in the reach being split into six flight blocks (Table 1), which were
 218 spaced longitudinally along the valley bottom. Flight lines were orientated
 219 in a traverse direction along the valley bottom (approximate maximum for
 220 DJI M300 RTK aircraft with L1 solid-state LiDAR sensor payload; 40 mins
 221 covering up to 0.4 km²). These separate flights were subsequently merged
 222 at later processing stages.

223
 224 Table 1: Flight Parameters, Point Counts & Densities for UAV LiDAR data
 225 collection

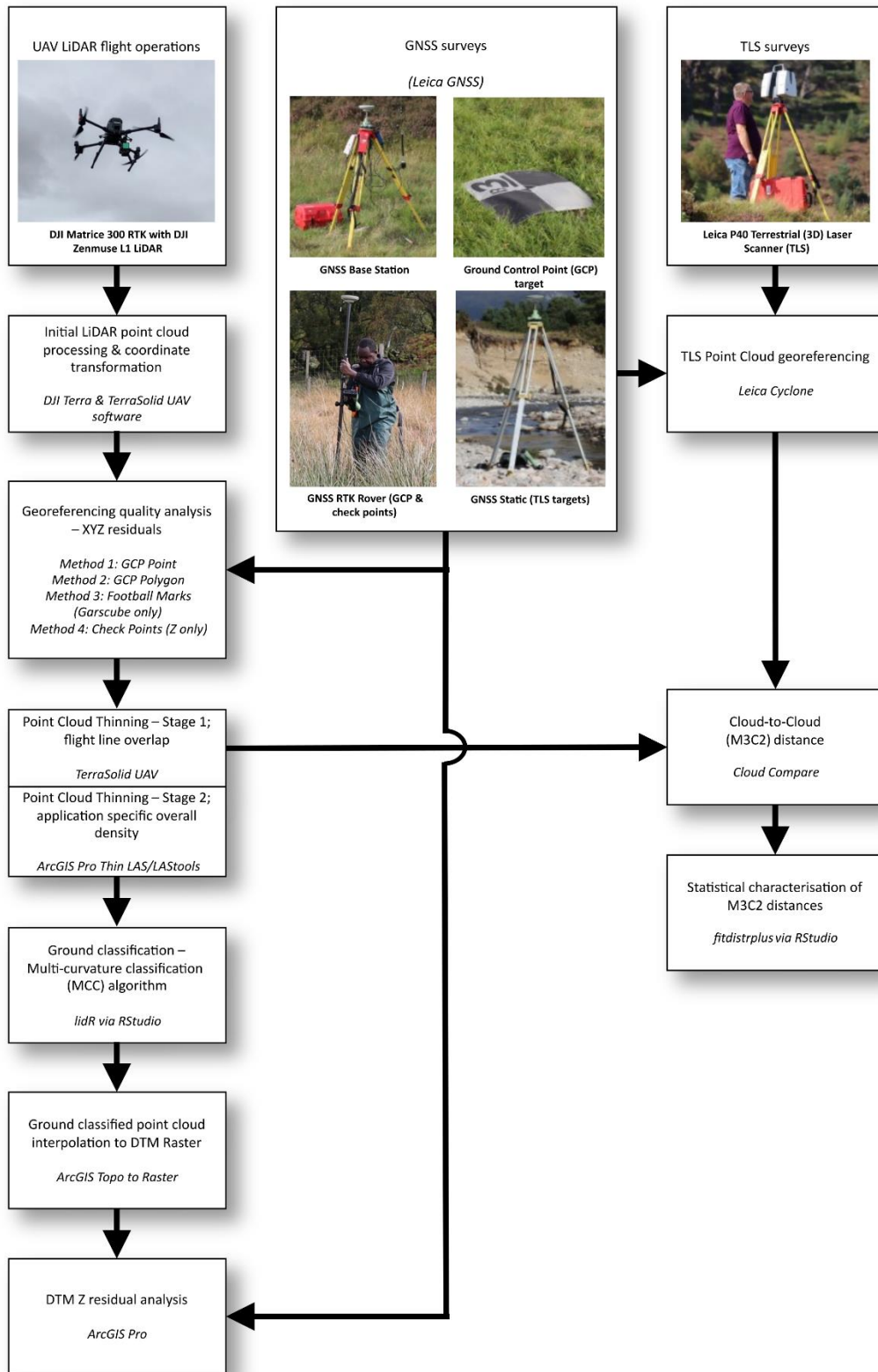
Flight Blocks	Flight Parameters		Pre-processing		Post-thinning	
	Flying Height (m above takeoff)	Speed (m/s)	Initial Number of Points	Point Density (pts/m ²)	Thinned Number of Points	Point Density (pts/m ²)
Garscube 1	80	5	7,948,865	645	1,576,001	128
Garscube 2	60	5	10,994,366	887	1,369,374	111
Garscube 3	60	10	5,803,970	470	1,359,296	110
Garscube 4	80	10	4,262,304	346	1,165,226	95
Feshie 1	70	10	167,801,385	403	32,417,397	82
Feshie 2			153,049,016	370	27,223,825	66
Feshie 3			76,774,455	341	16,411,617	73
Feshie 4			111,741,189	343	23,009,919	73
Feshie 5			79,409,092	333	17,002,397	71
Feshie 6			166,018,675	358	27,331,428	62

226
 227 **3.2 - GNSS data collection**
 228 Twenty-six chessboard pattern Ground Control targets were laid in a semi-
 229 regular pattern across the Garscube sports pitch (Figure 1b) and measured
 230 with a Leica Viva GS08 survey-grade RTK-GNSS, positioned with a tripod
 231 for stability. Furthermore, an extra 48 points were collected at distinct

232 sports pitch markings (e.g. at corners; Figure 1b). All the GNSS points
233 collected used the nearby GLAS reference station across Leica SmartNet
234 mobile network corrections, resulting in an average horizontal and vertical
235 quality of < 1 cm for the Ground Control targets, and slightly larger, c. 1
236 cm for the measurements of sports pitch marks.

237

238 Thirty-four GCPs were laid across the Feshie study area to provide XYZ
239 quality checks (Figure 1c – 1e). These targets were positioned using a Leica
240 1200 Series RTK-GNSS unit with a tripod for stability. The Feshie GNSS
241 points were corrected using a Leica GS16 in base station mode located over
242 a well-established ground mark that has been used in previous surveys.
243 This resulted in average reported point qualities of < 1 cm in both horizontal
244 and vertical. In equivalency to the football markings, a large sample of
245 points was collected along most of the main estate vehicle tracks within the
246 study site as well as along the dry gravel sections of the river channel area
247 using RTK-GNSS without a tripod and a shorter occupancy (Figure 1c – 1e).
248 Furthermore, sample points were taken within five types of vegetation
249 cover (grass, heather, sparse tree, dense trees, and high bars with moss)
250 to enable assessment of the LiDAR in vegetated areas (Figure 1c – 1e).



251
252
253
254
255
256
257

Figure 2: Data collection and data processing workflow diagram. The three columns (UAV flight operations, GNSS surveys, TLS surveys) represent the main techniques of data collection. TLS surveys were used on this investigation as a rigorous accuracy check, but subsequent surveys are unlikely to use this technique to assess the quality of a Digital Terrain Model produced from UAV LiDAR.

258 **3.3 - UAV LiDAR data processing**

259 The Garscube datasets were used to develop a data processing workflow
260 from the point cloud through to an output Digital Terrain Model (DTM;
261 Figure 2); this workflow was subsequently applied to process the River
262 Feshie data. The data were first processed in DJI Terra software to create
263 an initial LAS point cloud file and flight path trajectory files. In this step,
264 processing involved the initial georeferencing of the point cloud, based on
265 the RTK-GNSS onboard the aircraft (direct georeferencing; Dreier et al.,
266 2021), using the Optimise Point Cloud Accuracy setting. The point cloud
267 was then exported in WGS84 latitude and longitude coordinates with
268 ellipsoidal heights. Next, the data were imported into TerraSolid software
269 and processed using the Drone Project wizard in the TerraScan module. In
270 this step, the LAS file output from DJI Terra, as well as flight path trajectory
271 files, were projected to a local coordinate system: OSGB36(15) British
272 National Grid (EPSG:27700) for horizontal position and Ordnance Datum
273 Newlyn (ESPG:5701) for orthometric height.

274
275 The point cloud data were thinned (Resop et al., 2019) using two processes
276 to reduce and balance the point density such that processing over larger
277 areas (e.g. Feshie study area = c. 1.5 km²) did not become computationally
278 cumbersome due to the high point densities (Table 1). Firstly, overlapping
279 points captured whilst flying along adjacent flight lines were removed using
280 a tool in the TerraScan Process Drone Data wizard which establishes the
281 closest overlapping point relative to the nearest flight line and discards the
282 other overlapping points, thereby minimising noise in these overlap areas.
283 The data were then further thinned using the Thin LAS tool in ArcGIS Pro
284 to reduce the point density to a point every 15 cm in both the horizontal
285 and vertical, which approximated the required resolution for the
286 geomorphological context of the survey. A similar open-source tool is
287 available through LASTools (rapidlasso GmbH, 2021).

288

289 **3.4 - XYZ residual analysis: GCPs**

290 Two methods were used to select LiDAR points from each pre-thinned point
291 cloud for comparison to the known GNSS coordinates in all three
292 dimensions (Easting/Northing/Height). First, a point-to-point method,
293 referred to hereafter as *GCP Point*, was used to digitise a point selection at
294 the centre of the ground target in the displayed LAS file in ArcGIS Pro
295 software. This is similar to the method to GCP selection in SfM
296 photogrammetric processing (e.g. with Pix4D software; Stott et al., 2020).
297 The second point-to-point method, referred to hereafter as *GCP Polygon*,
298 was used to digitise a polygon of the extent of the ground control target (c.

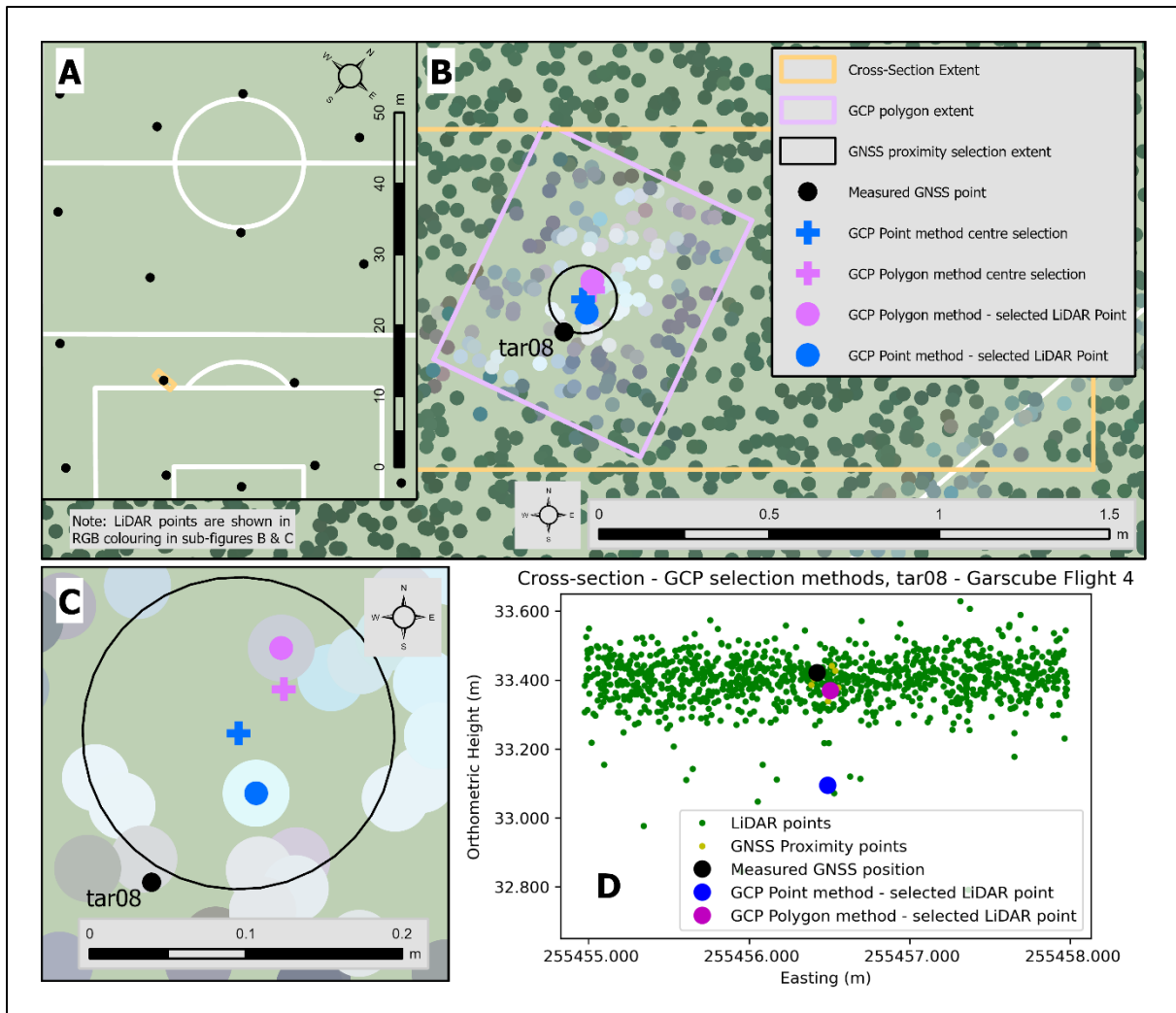
299 0.61 m x 0.61 m) from the displayed LAS data. The centre point of the
300 digitised polygon was calculated and used as the single selection point. At
301 Garscube, the additional GNSS measurements taken on the football pitch
302 markings were also used for residual analysis. The centre of the intersecting
303 pitch lines (pitch lines were 0.114 m wide) were used to digitise a point at
304 this location, in the same manner as the *GCP Point* method. This analysis
305 will be hereafter referred to as *Football Marks*. For all three of these
306 methods, the LiDAR coordinates from the pre-thinned point clouds were
307 subtracted from the GCP coordinates to determine the individual residual
308 for that GCP in each dimension, and summary statistics were calculated for
309 each flight.

310

311 **3.5 - Z residual analysis: GCPs and check points**

312 Upon initial inspection of some of the orthometric height results from the
313 point-to-point methods described above, some significantly larger residuals
314 were identified. Some investigation determined that it was caused when
315 the selected LiDAR point was not quite representative of the local sample
316 of points and their recorded orthometric heights (Figure 3d). Therefore, a
317 further method of residual analysis was devised (Mayr et al., 2019) which
318 used a sample of the LiDAR points located within a 0.1 m radius of the
319 selected location (GCP or check point) to enable the calculation of the mean
320 average of the orthometric height of the LiDAR points within this search
321 radius prior to differencing with the measured GNSS height. This method is
322 herein referred to as *GNSS Proximity* (Figure 3b/3c). For the Feshie, the
323 additional GNSS measurements along the vehicle tracks, dry river bars and
324 in vegetation were used to supplement the GCPs and provide further data
325 to assess the vertical consistency of the LiDAR data across a variety of
326 surface types.

327



328
 329 Figure 3: Selection of LiDAR point for Z residual calculation using point-to-
 330 point comparison methods. a) Location of measured GNSS (GCP target)
 331 points across Garscube football pitch. b) GCP location in RGB-coloured
 332 point cloud with cross-section, digitised target extent, and various point
 333 locations. c) An inset around the centre of GCP target showing the two
 334 LiDAR points selected as nearest to centre selections for *GCP Point* and
 335 *GCP Polygon* methods, as well as the extent of GNSS Proximity selection
 336 ($n=8$ for this target). d) Cross-section of point cloud showing how the
 337 selection of nearest LiDAR point (*GCP Point* or *GCP Polygon* methods)
 338 can result in non-representative Z location and an outlier residual, with
 339 *GNSS Proximity* method performing better since the selected point(s) are closer
 340 to the position measured by RTK-GNSS.

341
 342 **3.6 - Ground classification and DTM creation**

343 Digital Terrain Models (DTMs) were created from the Garscube and Feshie
 344 point cloud data. For Garscube, a DTM was created for each of the four test
 345 flights, and in the Feshie a single DTM created from the combination of the
 346 six individual DTMs for each flight block.

348 To create a DTM from the point cloud, it first needed to have a subset of
349 points classified as ground returns. The lidR library (Roussel & Auty, n.d.;
350 Roussel et al., 2020) within R software (R Core Team, 2021) was used to
351 classify ground returns in the point cloud. This library was used to test
352 different input parameters and ground classification algorithm options,
353 using the Garscube Flight 1 dataset and part of the Feshie point cloud. The
354 tests were undertaken for three algorithm options: the Cloth-Simulation
355 Function (CSF; Zhang et al., 2016); Progressive Morphological Filter (PMF;
356 Zhang et al., 2003); and Multiscale Curvature Classification (MCC; Evans &
357 Hudak, 2007). Once the MCC algorithm was chosen further testing using
358 various values for curvature and scale parameters was undertaken using
359 on Garscube and Feshie test areas. Default parameters identified by Evans
360 & Hudak (2007), scale (λ or s) of 1.5 and curvature (t) of 0.3, were used
361 based on the findings of these tests. Due to the intensity of computational
362 processing, each of the six River Feshie point clouds were processed
363 separately to extract a subset of ground classified points.

364

365 The ground classified point clouds (four at Garscube, six at Feshie) were
366 then interpolated into a raster DTM of 0.2 m resolution using the Topo to
367 Raster tool in ArcGIS Pro (Hutchinson, 1998; Smith et. al., 2003). Three
368 flight blocks at the Feshie were merged into a single interpolation meaning
369 only two halves needed merged, using the centre of the overlap zone
370 between Flight 3 & Flight 4. The Feshie and Garscube DTMs were then also
371 assessed for vertical accuracy against the known GNSS heights using data
372 from all the various surface and target types.

373

374 **3.7 - Terrestrial Laser Scanning comparison – River Feshie**

375 Terrestrial Laser Scanning (TLS) data collected at seven sample sites across
376 the River Feshie were used to quantify the M3C2 differences (Lague et al.,
377 2014) between the UAV LiDAR and the TLS point clouds (Babbal et al.,
378 2019; Dreier et al., 2021; Mayr et al., 2019). The seven samples varied in
379 spatial extent ($n = 148,687$ to $3,116,779$ point samples), but all focused
380 on gravel bar areas within the active river zone with vegetation and areas
381 outwith the control targets removed prior to further analysis.

382

383 The M3C2 differences were calculated in CloudCompare (CloudCompare,
384 2022) using the default algorithm and settings (Lague et al., 2013; TLS as
385 reference point cloud). The calculated M3C2 standard deviations were used
386 to visualise the minimum and maximum expected values for the M3C2
387 distributions. Subsequently, the seven samples were combined and the
388 overall M3C2 distribution was approximated empirically following the

389 procedure presented in Williams et al. (2020a). The fitdistrplus R-package
390 (Delignette-Muller & Dutang, 2015) was used to identify reasonable
391 candidate distributions and select the best-fit (Supplementary Materials C).

392

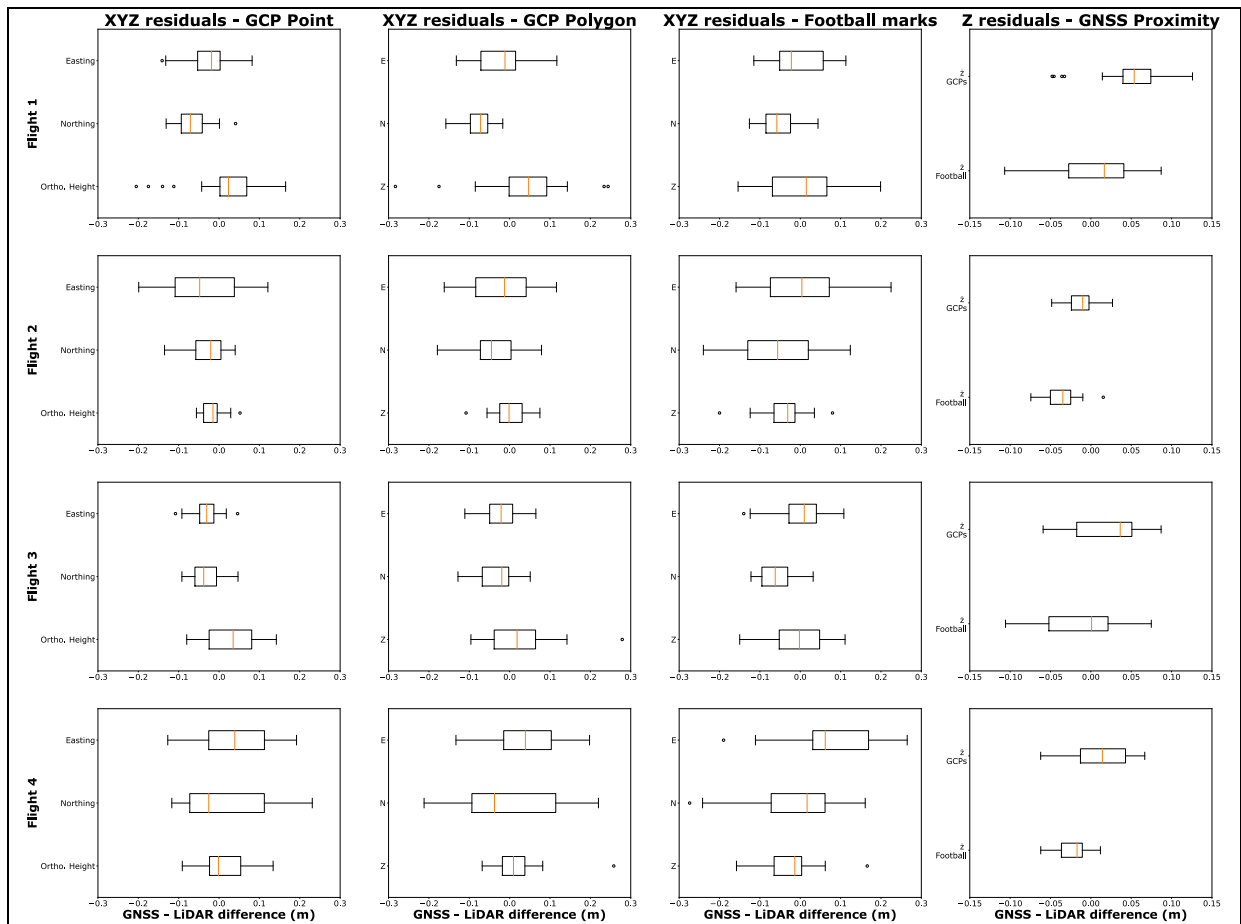
393 **4.0 - Results**

394

395 **4.1 - Garscube XYZ residual results**

396 Initial testing of the positional uncertainty of the DJI L1 solid-state LiDAR
397 system undertaken at the synthetic football pitch at Garscube
398 demonstrated sufficiently accurate and precise results with respect to both
399 the horizontal and vertical residuals. These results are summarised in
400 Figure 4 which shows the consistent centimetric-scale accuracy in all
401 dimensions across the four different flight tests, as well as the four different
402 *GCP Point, GCP Polygon, Football Marks and GNSS Proximity* residual
403 methodologies. The magnitude of the errors across the four flights and
404 three different comparison methods are mostly within several guideline
405 thresholds you could expect and consider for this type of data collection.
406 Firstly, the accuracy of the GNSS measurements (Supplementary Materials
407 A) used to calculate the positional residuals of the LiDAR data are
408 comparable. Secondly, considering the average point densities of the pre-
409 thinning point clouds (Table 1), the residual errors of the LiDAR data are
410 again of a similar magnitude as the spacing of LiDAR points (vary between
411 0.088 m (Garscube Flight 1) and 0.127 m (Feshie Flight 6) spacing between
412 LiDAR points).

413



414 Figure 4: Garscube GNSS-LiDAR residuals. Each row represents a
 415 different flight test (Table 1), and each column a different method for
 416 calculating the residuals. Note that the first three columns are for XYZ
 417 residuals, whilst the right column is the mean average of Z residuals, for
 418 the GCPs and Football Marking respectively.

419
 420 At Garscube, four flights were conducted with one of the objectives being
 421 to establish any significant difference between different flight parameters,
 422 namely flying height, and speed. These parameters influence the point
 423 density of the data, as well as the possible coverage area during a single
 424 flight or a larger survey campaign with multiple flights (Babbel et al., 2019;
 425 Resop et al., 2019). To establish if one of these combinations was optimal
 426 based on the above geometric residual results, the Easting, Northing and
 427 Orthometric Height residuals of the all the GNSS measurements for the four
 428 flights were statistically compared using a Kruskal-Wallis, non-parametric
 429 test. The results of these tests concluded no statistical difference between
 430 any of the flights for any of the three dimensions.

431
 432 Further investigation of the residuals shows minor variability between the
 433 flights in terms of the directionality of the various residuals calculated,
 434 notably in the Easting & Northing dimensions. However, the magnitude of

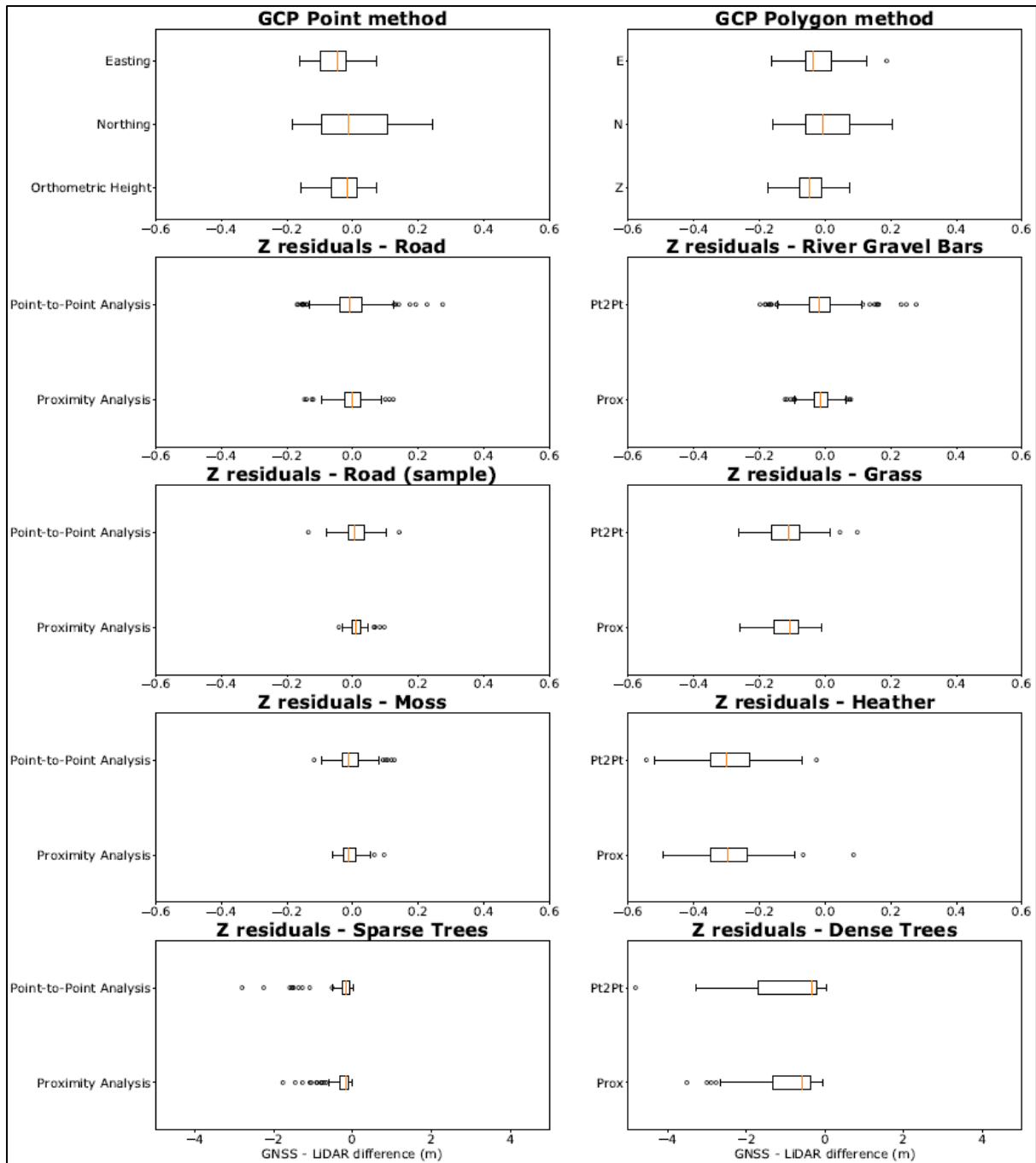
435 this variability was still minimal (c. 0.06-0.08 m) and remained within the
436 expected tolerances described above. Although the same programmed
437 flight path was used for all Garscube flights with the use of the D-RTK base
438 station for the aircraft, the actual flight paths displayed some minor
439 variability, which could be attributed to environmental conditions like the
440 light wind and associated corrections to maintain the flight path to the plan.
441 This variability in flight path may go some way to explaining the minor
442 variance between the different flights that are not explained by changes in
443 flying height and speed.

444

445 **4.2 - River Feshie XYZ residuals**

446 The magnitude and variability of the geometric residuals for the River
447 Feshie site (Figure 5) were comparable to those seen during the Garscube
448 testing, for non-vegetated areas (GCPs, Road, River Gravel). Residuals for
449 vegetated areas were, however, more complex. For these areas, in addition
450 to summarising geometric residuals for all the sample points (Figure 5),
451 Figure 6 shows representative cross-sections through the point cloud for
452 each vegetation type. The residuals of the pre-thinned point cloud in these
453 vegetated areas show significant offsets between the measured GNSS
454 points and selected point cloud data. However, all the trends in the
455 residuals are similar to the magnitude of the vertical dimensions of these
456 different vegetation types. For example, LiDAR data collected in areas with
457 moss (on gravel bars) had a mean average vertical residual of -0.007 m,
458 whereas areas of heather (without trees) had a mean average offset of -
459 0.290 m. With respect to the latter, this is indicative of the LiDAR
460 measurements not penetrating through heather to the ground level, which
461 can be seen in a representative cross-section through the point cloud for
462 this vegetation type (Figure 6). Residuals for grass are similar to those
463 associated with heather, albeit of a smaller magnitude (-0.116 m), most
464 attributable to the lesser density of the vegetation structure. For canopy-
465 type vegetation, residuals demonstrate that the LiDAR is capable of partial
466 penetration through sparse trees but not dense trees; the mean average
467 vertical residuals were respectively -0.297 m and -0.883 m for these
468 vegetation types.

469

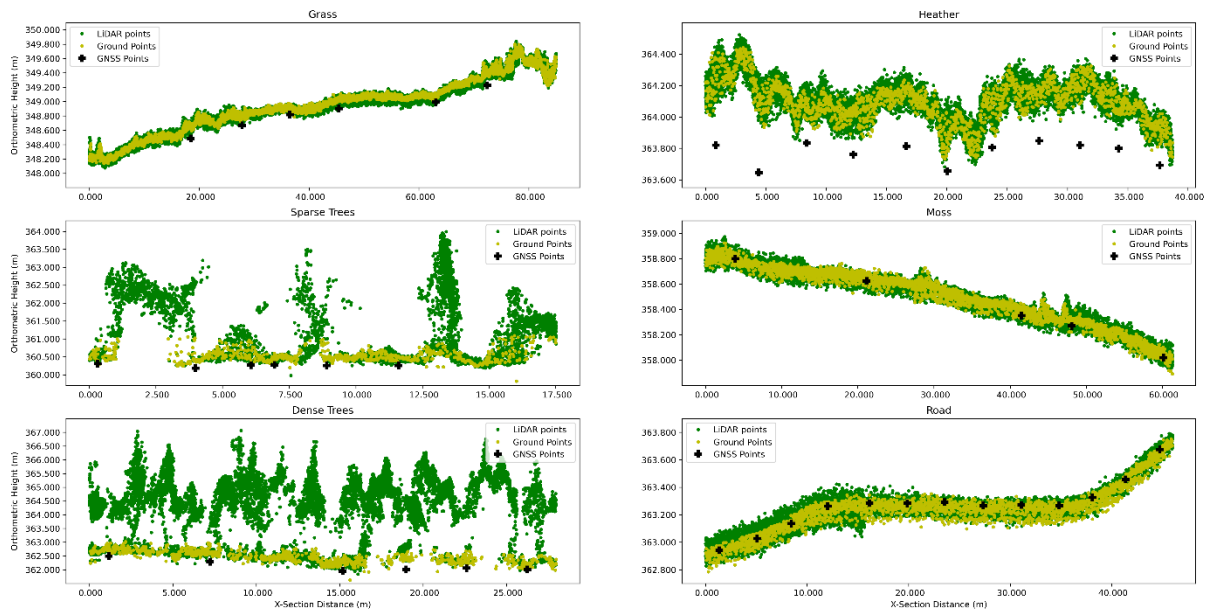


470
 471
 472
 473
 474
 475

Figure 5: Feshie GNSS-LiDAR residuals. The first row shows the XYZ residual results when using the GCP Point and GCP Polygon methods. Row 2 and below shows Z residuals for the various measured check points throughout the Feshie using both the point-to-point method and also an average of the LiDAR points within immediate proximity.

476
 477
 478

Figure 6 shows several cross-sections from the different vegetated areas, showing how the LiDAR penetrated through canopy-type vegetation, but could only capture the top surface of denser vegetation types like heather.



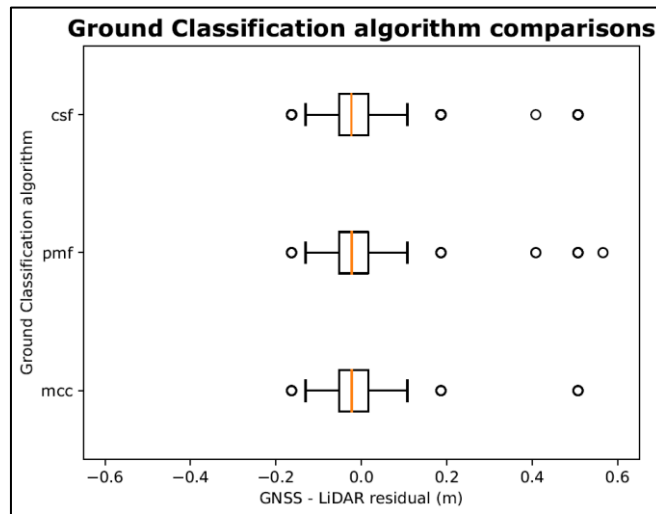
479
 480 *Figure 6: Example 1 m wide cross-section through the vegetated areas of*
 481 *the LiDAR survey. GNSS measured points shown by blue crosses show the*
 482 *lack of penetration of LiDAR measurements through dense vegetation*
 483 *(e.g., Heather), whilst on less dense vegetation (e.g., Moss) or hard*
 484 *features (e.g., Road) the GNSS measurements are centred within the*
 485 *LiDAR measurements.*

486 **4.3 - Ground Classification and DTM creation**

487 Ground classification is a key step to produce a realistic terrain product for
 488 further use. Therefore, particular attention was paid to selecting the best
 489 algorithm and parameters for the variety of features seen in vegetated
 490 fluvial environments.

491
 492 Three different ground class algorithms and a range of associated
 493 parameters were tested on Garscube Flight 1 and a test area within the
 494 River Feshie site. This resulted in 146 test point clouds being created, with
 495 nearly 2,500 residual calculations. These residuals were then tested to see
 496 if there was any statistically significant difference between any of the
 497 algorithms across all parameter settings. Figure 7 shows the distribution of
 498 residuals plotted for each algorithm, and almost no difference can be seen
 499 between them. All three algorithms converge around minimal to no
 500 elevation residual when compared against the GNSS measurements. The
 501 performance of the three algorithms could not be statistically separated.
 502 The Multi-Curvature Classification (MCC) algorithm was chosen (using $\lambda =$
 503 1.5 and $t = 0.3$ as input parameters) for this ground classification for two
 504 reasons. First, it gave the best qualitative result by removing non-ground
 505 features like buildings and trees from the test sites used. Secondly it also
 506 did not remove too much data, resulting in large holes in the point cloud

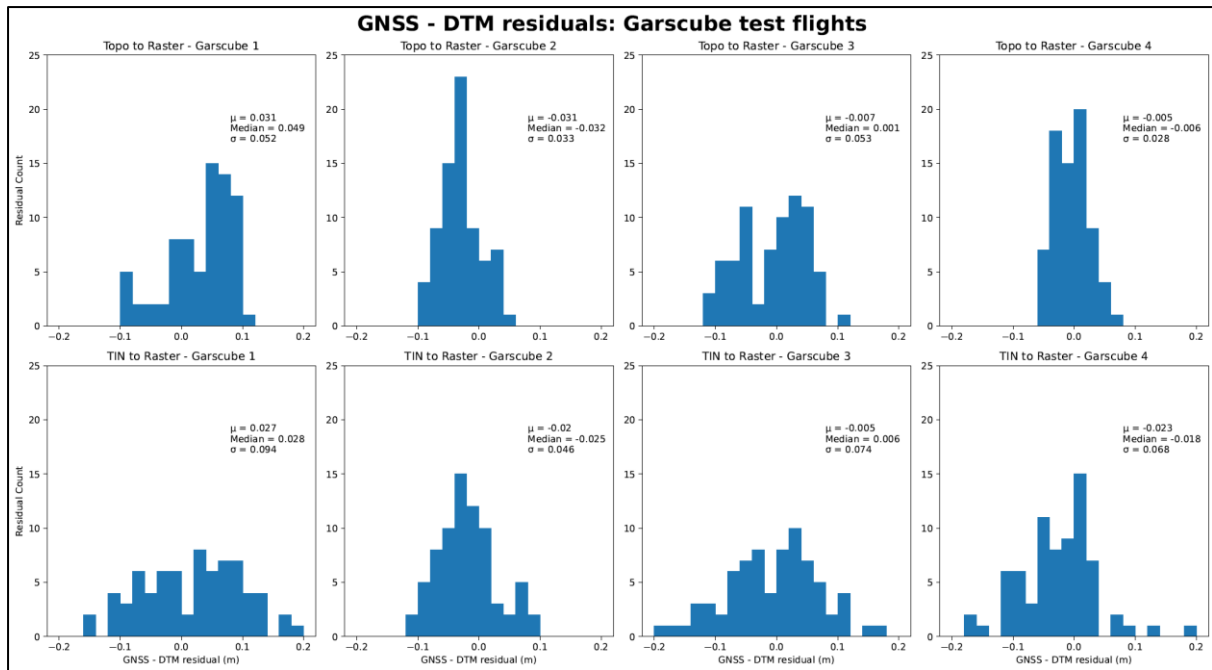
507 that were associated with other alternative algorithms and parameter
508 settings.



509
510 *Figure 7: Boxplots for each of the three ground classification algorithms*
511 *trialled using the lidR coding package (J. R. Roussel et al., 2020).*
512 *Residuals are combined from both the Garscube and the Feshie test site,*
513 *for all parameter settings combined.*

514 Converting point cloud data into continuous gridded raster products
515 required an appropriate interpolation method. Further analysis was
516 undertaken with all four Garscube flights, comparing the Topo to Raster
517 interpolation, available in ESRI ArcGIS products (Hutchinson, 1989; Smith
518 et al., 2003) and another common methodology in geomorphological
519 applications, converting point data via a Triangulated Irregular Network
520 (TIN) to raster.

521
522 Quantitative analysis of the DTM residuals from the GNSS measurements
523 (Figure 8) across the football pitch showed no obvious difference between
524 the methods. However, Topo to Raster interpolation had a tighter
525 distribution of residuals (indicated by the standard deviations, Figure 8)
526 across all four flights, despite the mean and median of some flights being
527 lower for the TIN to Raster method. Consequently, Topo to Raster was
528 chosen with no drainage corrections applied.



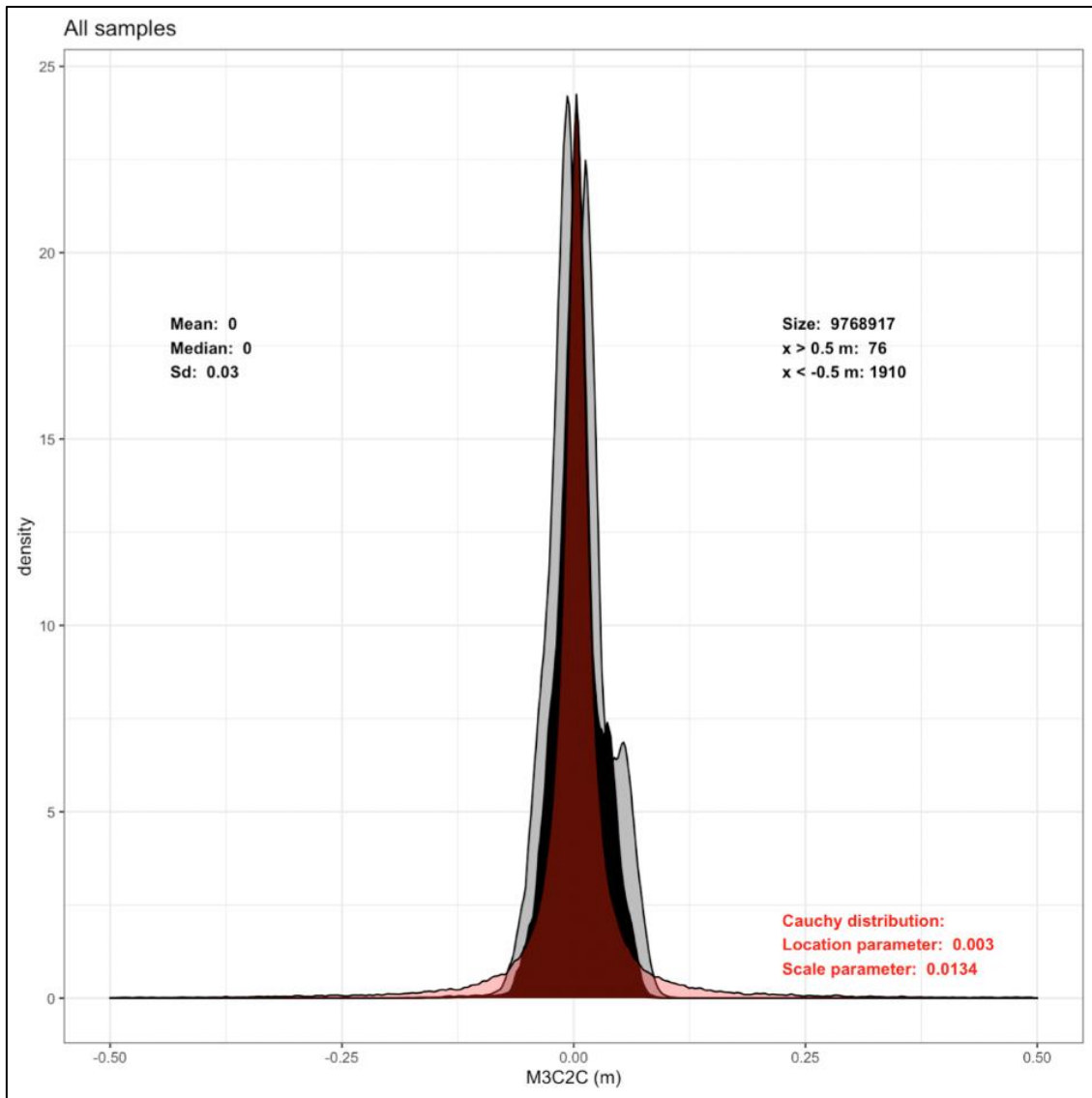
529

530 *Figure 8: Testing of two interpolation methods across all four Garscube*
 531 *test flights. Topo to Raster interpolation (top row) and TIN to Raster*
 532 *interpolation (bottom row).*

533 **4.4 - M3C2 differences**

534 The local M3C2 calculations for the seven sample sites, which compared
 535 the UAV LiDAR and TLS point clouds, showed the dominance of marginally
 536 zero M3C2 residual values for the all the sub-areas. The mean M3C2
 537 residuals ranged from -0.02 m to 0.05 m respectively, with equally low
 538 median residuals varying between -0.01 m to 0.05 m and tight standard
 539 deviations of these M3C2 residual distributions between 0.02 m and 0.04
 540 m. Outlier residuals, defined as M3C2 differences greater than 0.5 m, were
 541 also minimal across all the sample site, only representing between 0.007%
 542 and 0.04% of the local samples.

543 The distribution fitting shows how a Cauchy distribution (location parameter
 544 = 0.003; scale = 0.0134) outperforms the corresponding Gaussian fitting,
 545 for the approximation of the combined M3C2 difference from all areas
 546 (Figure 9). The latter is strong evidence for the marginally zero type of the
 547 M3C2 difference between the two point clouds (UAV LiDAR and TLS), since
 548 the Cauchy distribution is characteristically leptokurtic.



549

550 *Figure 9: The distribution of the combined M3C2 differences between the*
 551 *UAV-LiDAR and the TLS point clouds (River Feshie, black). The grey*
 552 *histograms demonstrate the maximum and the minimum expected*
 553 *distributions (M3C2-uncertainty and M3C2+uncertainty for left and right*
 554 *respectively). The red fitting, shows samples of the fitted Cauchy*
 555 *distribution as selected and approximated in Supplementary Materials C.*

556 **5.0 - Discussion**

557

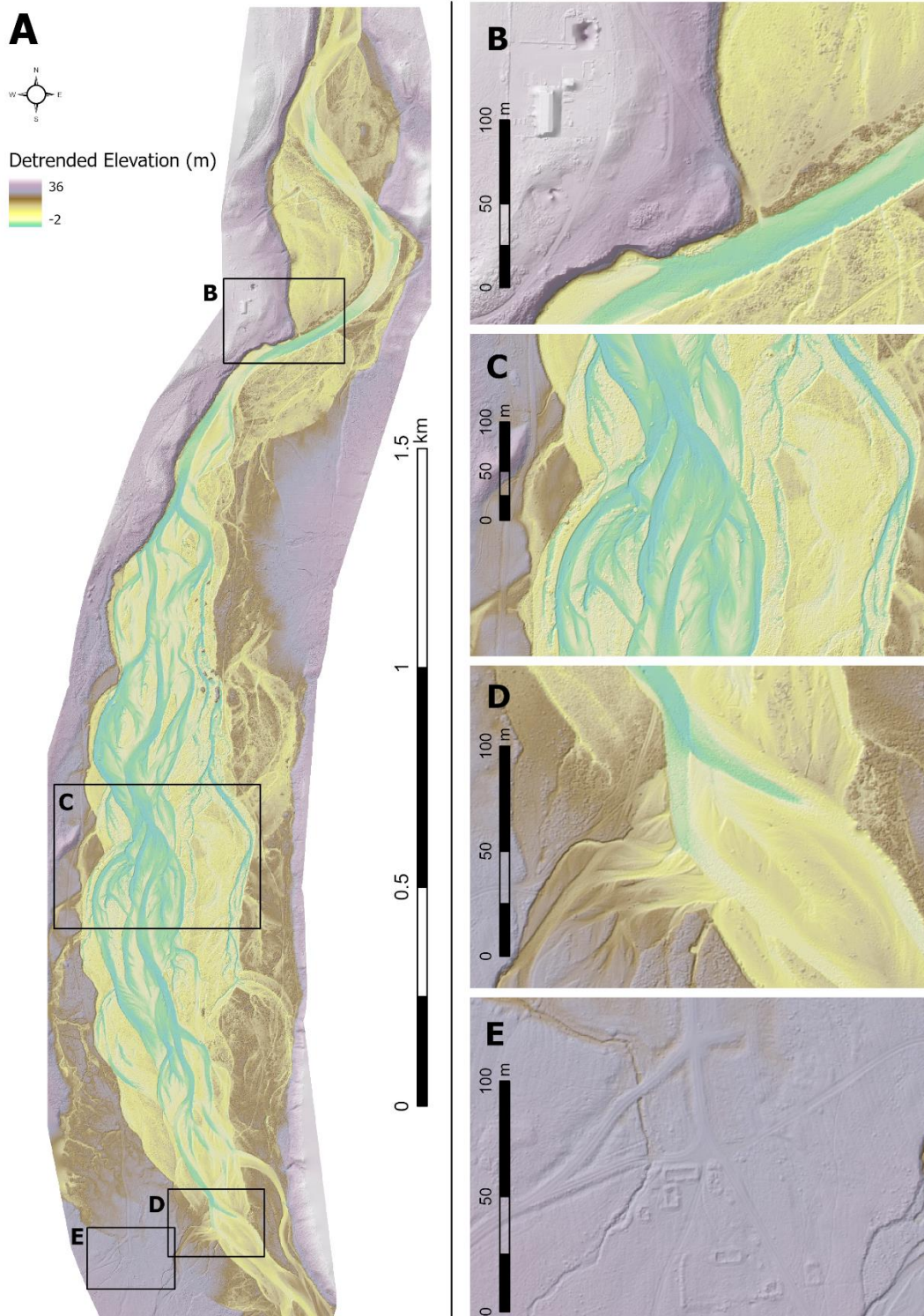
558 **5.1 – Reach-scale topography**

559

560 Figure 10A shows the reach-scale DEM of the River Feshie collected using
561 the DJI L1 solid-state LiDAR sensor in September 2021. This figure also
562 highlights particular areas of interest to illustrate the overall quality of the
563 topographic reproduction (Figures 10C and 10D), some areas where the
564 automated point cloud classification algorithm does not remove all surface
565 objects (Figure 10B) and where historic anthropogenic features can be
566 revealed (Figure 10E). The ground control and vertical check point error
567 assessments at the River Feshie demonstrate that the horizontal and
568 vertical accuracy of point data acquired by UAV solid state LiDAR is at least
569 comparable to equivalent surveys undertaken on the same reach using SfM
570 photogrammetry (Stott et al., 2020) and ground-based laser scanning
571 (Williams et al., 2014). The magnitude of the residuals are comparable to
572 the feasible level of detection in a fluvial gravel-bed river environment due
573 to the surface grain size. Moreover, the residuals must be considered within
574 the context of the LiDAR point spacing, which ranges from c. 0.034 m to
575 0.055 m for Garscube and the River Feshie respectively. These point
576 spacings are high for aerial topographic surveys but the inherent noise in
577 the point cloud data (Figure 6) will likely occlude opportunities for grain size
578 mapping from elevation distributions (Brasington et al., 2012; Pearson et
579 al., 2017; Reid et al., 2019).

580 The UAV solid state LiDAR to TLS point cloud comparison clearly indicates
581 marginally zero residuals in unvegetated areas. Thus, future geomorphic
582 applications of the DJI L1 solid-state LiDAR sensor need not conduct error
583 analysis assessment to the degree that has been undertaken here to
584 quantify horizontal and vertical residuals.

585 Although the workflow is not fully streamlined into one software application,
586 it is both reproduceable and modifiable. Indeed, since data collection and
587 processing of the Garscube and River Feshie datasets, updates to DJI Terra
588 software could further streamline the processing workflow with respect to
589 coordinate conversions datums and point cloud densities.



590

591 *Figure 10: (A) DEM of the 3 km long River Feshie reach, with hillshade*
 592 *illumination and linearly detrended by longitudinal valley slope. Insets*
 593 *shows areas of interest: (B) artefacts of estate buildings and vegetation*
 594 *not removed through automated point classification process; C)*
 595 *anabranches; D) confluence of Shlochd Beag and River Feshie; E)*
 596 *footprints of demolished estate buildings under grass cover revealed by*
 597 *LiDAR DEM and hillshade.*

598 **5.2 – Vegetation and bathymetry**

599 An advantage of using active remote sensing techniques, such as LiDAR, is
600 their penetration of vegetation and thus the ability to derive a bare earth
601 DTM instead of vegetated DSM. In this paper we demonstrate that the error
602 in vegetated areas varies (-0.007 m to -0.883 m; Figures 5 and 6)
603 depending upon the density of vegetation. Several other investigations
604 (e.g. Babbel et al., 2019; Crow et al., 2007; Evans & Hudak, 2007;
605 Javernick et al., 2014; Resop et al., 2019) have found similar limitations
606 related to ground/vegetation classification related to vegetation density,
607 particularly the presence of dense understory vegetation which significantly
608 reduced LiDAR penetration to ground level. To obtain a true ground
609 measurement the laser pulse from the instrument has to pass through any
610 canopy and understory vegetation in both directions (i.e. away from the
611 sensor and on return). This can be considered partially a function of the
612 LiDAR sensor's power specification. The DJI L1 solid-state LiDAR sensor
613 produces around 30W with a maximum of 60W; our investigation has
614 demonstrated the capabilities of this sensor for penetrating sparse
615 vegetation and the limitations for penetrating dense vegetation. Several
616 authors have described potential considerations which may improve data
617 collection using LiDAR in vegetated areas including a methodology for
618 canopy and ground penetration estimation, scan angle including overlap
619 percentage (Babbel et al., 2019; Crow et al., 2007) and field-of-view,
620 seasonal flying during winter period with less foliage (Crow et al., 2007;
621 Resop et al., 2019), and flight orientations in areas of linear vegetation
622 growth (e.g. plantation forests; Crow et al., 2007). For types of vegetation
623 that are similar to those found in the River Feshie, further experiments
624 could be conducted to assess improvements to vegetation penetration by
625 flying lower, increasing the flight overlaps to >50%, changing the scanning
626 pattern, altering point cloud thinning to ensure more oblique points
627 originating from an adjacent flight line with the field-of-view are used more,
628 and flying after autumnal foliage dieback. The latter is, however, species
629 specific and would not overcome problems with heather since it does not
630 dieback. Overall, it is thus recommended that users always conduct a pre-
631 survey investigation of their site to assess the best approach to minimise
632 errors arising from dense canopy and/or understory vegetation.

633 A key limitation of the DJI L1 solid-state LiDAR is that ground returns are
634 only obtained from dry topography; wet areas such as rivers and ponds
635 have reduced or erroneous returns (Babbel et al., 2019; Resop et al.,
636 2019). There are three approaches that could be applied to reconstruct the
637 topography of wet areas, which could subsequently be fused (Williams et
638 al., 2014) into the dry bare earth DTM. First, wet topography could be
639 directly surveyed using robotic total station, RTK-GNSS or echo-sounding
640 (e.g. Williams et al., 2014; Williams et al., 2020b). Second, RGB images

641 that are acquired as part of the DJI L1 solid-state LiDAR survey, to colourise
642 the point cloud, could be used to produce an orthomosaic image and depth
643 could then be reconstructed using spectrally based Optimal Band Ratio
644 Analysis (OBRA; Legleiter et al., 2009); a technique that has been
645 operationalised by Legleiter (2021) in the Optical River Bathymetry Toolkit
646 (ORByT). This approach requires glint-free images, or images with glint
647 removed (Overstreet & Legleiter, 2017), and independent depth
648 observations to select the band ratio that yields the strongest correlation
649 between depth and the image-derived quantity. Finally, the third approach
650 is to acquire a set of RGB images from the UAV platform that can be
651 processed using SfM photogrammetry and then corrected for light
652 refraction through the water column using either a constant refractive index
653 (Woodget et al., 2015) or by deriving refraction correction equations for
654 every point and camera combination in a SfM photogrammetry point cloud
655 (Dietrich, 2017). All three approaches require water surface elevation to be
656 reconstructed before bed levels are calculated; this requires diligence and
657 can be a source of significant error (Williams et al., 2014; Woodget et al.,
658 2019). Of these three approaches, optical empirical bathymetric
659 reconstruction requires the least additional data collection and processing;
660 direct survey involves time-consuming ground-based sampling whilst
661 bathymetric correction techniques require images and computational
662 overheads associated with SfM photogrammetry. All these techniques are
663 widely established and have been applied to a range of rivers; it is thus
664 beyond the scope of our investigation to demonstrate these techniques
665 here for the Feshie.

666 **5.3 - Best practice recommendations**

667 Table 2 presents a set of ten best practice recommendations based on our
668 experience of deriving a bare earth DTM of the River Feshie using UAV solid-
669 state LiDAR. The recommendations are organised around the key steps in
670 the workflow that was developed and applied in this investigation. The first
671 three items relate to surveying considerations. Flight planning
672 considerations include the choice of the UAV navigation app and how the
673 UAV will be operated. The length of flight lines needs to stay within relevant
674 UAV flying laws and guidance. This may also be influenced by sensor
675 requirements; for example, the DJI L1 solid-state LiDAR sensor requires
676 flight line length to be <1000 m so that the IMU is regularly calibrated
677 during turning. For large survey areas, such as the 3 km River Feshie
678 reach, battery logistics becomes important as flight duration is greater than
679 the power that one set of batteries can provide (Resop et al., 2019);
680 locations for flight landing and take-offs to replace batteries need to be
681 accessible and planned. Sensor operation considerations are closely related
682 to flight planning considerations. Flight lines need side overlap of at least
683 50% but increasing overlap too much, for example to the 80% suggested

684 for SfM photogrammetry (James et al., 2019; Woodget et al., 2015), will
685 result in much longer flight times. Flying lower and slower yield a higher
686 sampling rate and thus greater point density but this increased sampling
687 rate will result in the use of more battery power. A choice also needs to be
688 made about the number of results to record; the L1 sensor's single outgoing
689 plus can be received as triple returns. Although not investigated here, these
690 returns can be analysed to characterise vegetation type and density (Resop
691 et al., 2019; Wallace et al., 2012). The third consideration is the acquisition
692 of independent survey data. Appropriate equipment (e.g. RTK-GNSS, total
693 station, TLS) needs to be deployed to sample surfaces that are subjected
694 to error analysis.

695 The fourth and fifth considerations are coordinate transformation and cloud
696 thinning. Raw point cloud data need transformation if output in a local or
697 national coordinate system is required. In this investigation, TerraSolid
698 software was used to transform the raw point cloud into the required
699 coordinate system, British National Grid (BNG). However, a recent software
700 update to DJI Terra now offers transformation to BNG, which simplify this
701 processing workflow. Point cloud thinning needs to consider the point
702 density that is required as output, possibly based off gridded DTM
703 resolution, and the algorithm that is subsequently used to thin both overlap
704 and the overall point cloud.

705 Consideration seven concerns the approach to point classification; a key
706 step in the process of deriving a high-quality DTM since this determines
707 which points are selected to represent bare earth. This investigation trialled
708 146 separate algorithms and parameter settings combinations before
709 settling on the default Multi-Curvature Classification (MCC) algorithm
710 (Evans & Hudak, 2007). This algorithm was specifically developed for
711 natural, forested areas. This contrasts with classification approaches for
712 more anthropogenically developed areas, where sharper curvature (e.g.
713 building walls, roofs) are considered, as opposed to softer curvature with
714 topography and vegetation. As the name suggests, MCC utilises a curvature
715 threshold method to assess and classify ground versus non-ground returns
716 at multiple scales within a local neighbourhood. Haugerud and Harding
717 (2001) developed a similar curvature-based classification algorithm known
718 as Virtual DeForestation (VDF) and suggested that the curvature tolerance
719 parameter (t) should be set at around four times the interpolated cell size.
720 Based on scale of sediment features in the River Feshie requiring a spatial
721 resolution of around 20 cm for geomorphological analyses, an appropriate
722 curvature tolerance of 0.8 was trialled for the various algorithms. This was
723 found to be quantitatively inseparable from residuals obtained from other
724 parameters but appeared qualitatively inferior to other settings, particularly
725 those outlined by Evans and Hudak (2007) and other lidR package
726 documentation. Sinkhole type artefacts, seen in some of our early test

727 results with other anthropogenically focused algorithms (e.g. in TerraSolid),
 728 were elucidated in Evans and Hudak (2007) as negative blunders resulting
 729 from scattering of the LiDAR pulses. The sinkhole artefacts tended to be
 730 most obvious on harder surfaces such as road and gravel bars, due to the
 731 uniformity of these surfaces. These sinkholes appeared to result from
 732 commission errors (classifying non-ground point as ground, false positive)
 733 using erroneous points that were below the actual ground and caused these
 734 significant artefacts in the first tests of gridded raster terrain model
 735 outputs. These sinkhole artefacts did not appear to be replicated in the
 736 more natural algorithms like MCC, which was used in the final product,
 737 although anthropogenic areas (e.g. farm buildings, Figure 10B) did have
 738 artefacts that were of less concern given the topographic context.

739 Item eight considers the algorithm choice to interpolate to a raster. Item
 740 nine focuses on accuracy assessment. At the same stage as flight and
 741 independent survey data planning, the accuracy assessment requirements
 742 need to be considered. It is recommended that these are split into three
 743 stages: pre-processing to assess the survey; post-processing to assess the
 744 ground classification; and raster interpolation to assess the gridded
 745 product. Finally, the approach to reconstructing wet areas, if required,
 746 needs to be determined. Options are discussed above, in Section 5.2, and
 747 may influence flight planning and a need to acquire depth data.

748 Table 2: Best practice recommendations for acquiring and processing UAV
 749 solid state LiDAR

Item	Considerations
1. Flight planning	<ul style="list-style-type: none"> • Choice of UAV. • Choice of UAV navigation app • Flight height, speed, direction. • Logistics for flight take-off and landing, including battery duration and battery swapping.
2. Operation of sensor	<ul style="list-style-type: none"> • Choice of sensor • Swath width and side overlap (50%). • Number of returns to record. • Sampling rate. • Calibration of IMU.
3. Independent survey data	<ul style="list-style-type: none"> • Distribution and number of independent points (e.g. targets, landscape features) to independently survey • Choice of equipment for accuracy assessment e.g. RTK-GNSS / total station / TLS.
4. Coordinate transformation	<ul style="list-style-type: none"> • Coordinate system for data collection and output product.
5. Cloud thinning	<ul style="list-style-type: none"> • Methods to thin overlap and overall point cloud.
6. Point classification	<ul style="list-style-type: none"> • Selection of algorithm. • Definition of representative sample for accuracy assessment.

7. Manual point cloud editing	<ul style="list-style-type: none"> • <i>Likely optional but should be considered after evaluating point classification accuracy.</i>
8. Interpolation to raster	<ul style="list-style-type: none"> • Selection of algorithm e.g. Topo2Raster, TIN to Raster.
9. Accuracy assessment	<ul style="list-style-type: none"> • Selection of statistical methods during three stages: <ul style="list-style-type: none"> ○ (1) Pre-processing – survey assessment; ○ (2) Post-processing – classification assessment; ○ (3) Raster interpolation assessment.
10. Wet areas	<ul style="list-style-type: none"> • Selection of technique for reconstruction, if required. • Approaches available: <ul style="list-style-type: none"> ○ Direct survey (robotic total station, RTK-GNSS, echo-sounding); ○ Refraction correction of SfM photogrammetry derived point cloud; ○ Spectrally based Optimal Band Ratio Analysis.

750

751 **6.0 - Conclusion**

752 This investigation has evaluated a new consumer-grade UAV solid-state
753 LiDAR sensor for topographic surveying and geomorphic characterisation of
754 fluvial systems. Given that this new mode of LiDAR technology has mainly
755 been used out with topographic surveying until very recently (Kim et al.,
756 2019; Raj et al., 2020; Štroner et al., 2021), the importance of our
757 investigation lies in the extensive geolocation error evaluation across study
758 areas with different degrees of topographical complexity.

759 Our results suggest that, in unvegetated areas, the accuracy of the DJI
760 Zenmuse L1 solid-state UAV LiDAR system is comparable to other current
761 UAV or aerial-based methods such as SfM photogrammetry, and
762 statistically indistinguishable from detailed ground-based TLS surveys. It is
763 possible to produce DEMs that achieve sub-decimetre scale (<0.1 m)
764 geolocation accuracy from the RTK aircraft position alone, even when
765 surveying in fluvial environments that are characterised by “noise” from
766 surface roughness associated with sediment and sparse canopy-type
767 vegetation. However, the solid-state LiDAR sensor was unable to penetrate
768 dense ground-hugging vegetation like heather or thick grass, resulting in
769 elevation bias in areas characterised by these types of vegetation.

770 Our investigation provides an initial processing workflow for UAV solid-state
771 LiDAR data, when applied to vegetated parts of the Earth’s surface.
772 Although the workflow is currently discontinuous, using a variety of
773 different software to process and assess the dense point clouds that are
774 acquired using these sensors, further software development will likely
775 improve processing efficiency. This will enable the characterisation of the

776 topography, and objects such as vegetation, using the increased density of
777 data that UAV solid-state LiDAR provides, and the increasingly large areas
778 that can be surveyed with contemporary UAV platforms.

References

- 780 Abbasi-Moghadam, D., & Abolghasemi, M. (2015). Designing and
 781 implementation of pushbroom imaging payloads for a remote sensing
 782 satellite. *Optical and Quantum Electronics*, 47(11), 3491–3508.
 783 <https://doi.org/10.1007/s11082-015-0225-z>
- 784 Alho, P., Vaaja, M., Kukko, A., Kasvi, E., Kurkela, M., Hyyppä, J., Hyyppä,
 785 H., & Kaartinen, H. (2011). Mobile laser scanning in fluvial
 786 geomorphology: Mapping and change detection of point bars.
 787 *Zeitschrift Fur Geomorphologie*, 55, 31–50.
 788 <https://doi.org/10.1127/0372-8854/2011/0055S2-0044>
- 789 Babbel, B. J., Olsen, M. J., Che, E., Leshchinsky, B. A., Simpson, C., &
 790 Dafni, J. (2019). Evaluation of uncrewed aircraft systems' LiDAR data
 791 quality. *ISPRS International Journal of Geo-Information*, 8(12).
 792 <https://doi.org/10.3390/ijgi8120532>
- 793 Bakker, M., & Lane, S. N. (2017). Archival photogrammetric analysis of
 794 river–floodplain systems using Structure from Motion (SfM) methods.
 795 *Earth Surface Processes and Landforms*, 42(8), 1274–1286.
 796 <https://doi.org/10.1002/esp.4085>
- 797 Ballantyne, C. K., Black, A. R., Ferguson, R., Gordon, J. E., & Hansom, J.
 798 D. (2021). Scotland's Changing Landscape. In C. K. Ballantyne & J. E.
 799 Gordon (Eds.), *Landscapes and Landforms of Scotland* (pp. 97–114).
 800 Springer Nature Switzerland AG.
- 801 Brasington, J., Rumsby, B. T., & McVey, R. A. (2000). Monitoring and
 802 modelling morphological change in a braided gravel-bed river using
 803 high resolution GPS-based survey. *Earth Surface Processes and*
 804 *Landforms*, 25, 973–990.
- 805 Brasington, J., Vericat, D., & Rychkov, I. (2012). Modeling river bed
 806 morphology, roughness, and surface sedimentology using high
 807 resolution terrestrial laser scanning. *Water Resources Research*,
 808 48(11), 1–18. <https://doi.org/10.1029/2012WR012223>
- 809 Carrivick, J. L., Smith, M. W., & Quincey, D. J. (2016). *Structure from*
 810 *Motion in the Geosciences*. John Wiley & Sons, Inc.
- 811 CloudCompare. (2022). *CloudCompare (version 2.10.2)*.
 812 www.cloudcompare.org
- 813 Clubb, F. J., Mudd, S. M., Milodowski, D. T., Valters, D. A., Slater, L. J.,
 814 Hurst, M. D., & Limaye, A. B. (2017). Geomorphometric delineation of
 815 floodplains and terraces from objectively defined topographic
 816 thresholds. *Earth Surface Dynamics*, 5(3), 369–385.
 817 <https://doi.org/10.5194/esurf-5-369-2017>
- 818 Crosby, C. J., Arrowsmith, J. R., & Nandigam, V. (2020). Zero to a trillion:
 819 Advancing Earth surface process studies with open access to high-
 820 resolution topography. In *Developments in Earth Surface Processes*
 821 (Vol. 23, pp. 317–338). Elsevier. [https://doi.org/10.1016/B978-0-](https://doi.org/10.1016/B978-0-444-64177-9.00011-4)
 822 [444-64177-9.00011-4](https://doi.org/10.1016/B978-0-444-64177-9.00011-4)
- 823 Crow, P., Benham, S., Devereux, B. J., & Amable, G. S. (2007). Woodland
 824 vegetation and its implications for archaeological survey using LiDAR.
 825 *Forestry*, 80(3), 241–252. <https://doi.org/10.1093/forestry/cpm018>

- 826 Cucchiaro, S., Cavalli, M., Vericat, D., Crema, S., Llena, M., Beinat, A.,
827 Marchi, L., & Cazorzi, F. (2018). Monitoring topographic changes
828 through 4D-structure-from-motion photogrammetry: application to a
829 debris-flow channel. *Environmental Earth Sciences*, 77(18), 1–21.
830 <https://doi.org/10.1007/s12665-018-7817-4>
- 831 Delignette-Muller, M. L., & Dutang, C. (2015). fitdistrplus: An R package
832 for fitting distributions. *Journal of Statistical Software*, 64(4), 1–34.
833 <https://doi.org/10.18637/jss.v064.i04>
- 834 Dietrich, J. T. (2017). Bathymetric Structure-from-Motion: extracting
835 shallow stream bathymetry from multi-view stereo photogrammetry.
836 *Earth Surface Processes and Landforms*, 42(2), 355–364.
837 <https://doi.org/10.1002/esp.4060>
- 838 Dreier, A., Janßen, J., Kuhlmann, H., & Klingbeil, L. (2021). Quality
839 analysis of direct georeferencing in aspects of absolute accuracy and
840 precision for a uav-based laser scanning system. *Remote Sensing*,
841 13(18). <https://doi.org/10.3390/rs13183564>
- 842 Eltner, A., Kaiser, A., Castillo, C., Rock, G., Neugirg, F., & Abellán, A.
843 (2016). Image-based surface reconstruction in geomorphometry-
844 merits, limits and developments. *Earth Surface Dynamics*, 4(2), 359–
845 389. <https://doi.org/10.5194/esurf-4-359-2016>
- 846 Eschbach, D., Grussenmeyer, P., Koehl, M., Guillemin, S., & Schmitt, L.
847 (2021). Combining geodetic and geomorphic methods to monitor
848 restored side channels: Feedback from the Upper Rhine.
849 *Geomorphology*, 374, 107372.
850 <https://doi.org/10.1016/j.geomorph.2020.107372>
- 851 Evans, J. S., & Hudak, A. T. (2007). A multiscale curvature filter for
852 identifying ground returns from discrete return lidar in forested
853 environments. *IEEE Transactions on Geoscience and Remote Sensing*,
854 45(4), 1029–1038.
- 855 Glennie, C. L., Carter, W. E., Shrestha, R. L., & Dietrich, W. E. (2013).
856 Geodetic imaging with airborne LiDAR: The Earth's surface revealed.
857 *Reports on Progress in Physics*, 76(8). <https://doi.org/10.1088/0034-4885/76/8/086801>
- 859 Haugerud, R. A., & Harding, D. J. (2001). Some algorithms for Virtual
860 DeForestation (VDF) of LiDAR topographic survey data. *International
861 Archives of Photogrammetry Remote Sensing and Spatial Information
862 Sciences*, 34(3/W4), 211–218.
- 863 Hutchinson, M. F. (1989). A new procedure for gridding elevation and
864 stream line data with automatic removal of spurious pits. *Journal of
865 Hydrology*, 106(3–4), 211–232. [https://doi.org/10.1016/0022-1694\(89\)90073-5](https://doi.org/10.1016/0022-1694(89)90073-5)
- 867 Iglhaut, J., Cabo, C., Puliti, S., Piermattei, L., O'Connor, J., & Rosette, J.
868 (2019). Structure from Motion Photogrammetry in Forestry: a Review.
869 *Current Forestry Reports*, 5(3), 155–168.
870 <https://doi.org/10.1007/s40725-019-00094-3>
- 871 Islam, M. T., Yoshida, K., Nishiyama, S., Sakai, K., & Tsuda, T. (2021).
872 Characterizing vegetated rivers using novel unmanned aerial vehicle-

873 borne topo-bathymetric green lidar: Seasonal applications and
874 challenges. *River Research and Applications*, March, 1–15.
875 <https://doi.org/10.1002/rra.3875>

876 Jaakkola, A., Hyyppä, J., Kukko, A., Yu, X., Kaartinen, H., Lehtomäki, M.,
877 & Lin, Y. (2010). A low-cost multi-sensoral mobile mapping system
878 and its feasibility for tree measurements. *ISPRS Journal of*
879 *Photogrammetry and Remote Sensing*, 65(6), 514–522.
880 <https://doi.org/10.1016/j.isprsjprs.2010.08.002>

881 James, M. R., Chandler, J. H., Eltner, A., Fraser, C., Miller, P. E., Mills, J.
882 P., Noble, T., Robson, S., & Lane, S. N. (2019). Guidelines on the use
883 of structure-from-motion photogrammetry in geomorphic research.
884 *Earth Surface Processes and Landforms*, 44(10), 2081–2084.
885 <https://doi.org/10.1002/esp.4637>

886 James, M. R., & Robson, S. (2014). Mitigating systematic error in
887 topographic models derived from UAV and ground-based image
888 networks. *Earth Surface Processes and Landforms*, 39(10), 1413–
889 1420. <https://doi.org/10.1002/esp.3609>

890 Javernick, L., Brasington, J., & Caruso, B. (2014). Modeling the
891 topography of shallow braided rivers using Structure-from-Motion
892 photogrammetry. *Geomorphology*, 213, 166–182.
893 <https://doi.org/10.1016/j.geomorph.2014.01.006>

894 Jones, A. F., Brewer, P. A., Jonhstone, E., & Macklin, M. G. (2007). High-
895 resolution interpretative geomorphological mapping of river valley
896 environments using airborne LiDAR data. *Earth Surface Processes and*
897 *Landforms*, 32, 1574–1592. <https://doi.org/10.1002/esp.1505>

898 Joyce, K. E., Anderson, K., & Bartolo, R. E. (2021). Of course we fly
899 unmanned—we're women! *Drones*, 5(1), 2–5.
900 <https://doi.org/10.3390/drones5010021>

901 Kasvi, E., Salmela, J., Lotsari, E., Kumpula, T., & Lane, S. N. (2019).
902 Comparison of remote sensing based approaches for mapping
903 bathymetry of shallow, clear water rivers. *Geomorphology*, 333, 180–
904 197. <https://doi.org/10.1016/j.geomorph.2019.02.017>

905 Kim, T., Bhargava, P., Poulton, C. V., Notaros, J., Yaacobi, A.,
906 Timurdogan, E., Baiocco, C., Fahrenkopf, N., Kruger, S., Ngai, T.,
907 Timalina, Y., Watts, M. R., & Stojanovic, V. (2019). A Single-Chip
908 Optical Phased Array in a Wafer-Scale Silicon Photonics/CMOS 3D-
909 Integration Platform. *IEEE Journal of Solid-State Circuits*, 54(11),
910 3061–3074. <https://doi.org/10.1109/JSSC.2019.2934601>

911 Lague, D., Brodu, N., & Leroux, J. (2013). Accurate 3D comparison of
912 complex topography with terrestrial laser scanner: Application to the
913 Rangitikei canyon (N-Z). *ISPRS Journal of Photogrammetry and*
914 *Remote Sensing*, 82, 10–26.
915 <https://doi.org/10.1016/j.isprsjprs.2013.04.009>

916 Legleiter, C. J. (2021). The optical river bathymetry toolkit. *River*
917 *Research and Applications*, 37(4), 555–568.
918 <https://doi.org/10.1002/rra.3773>

919 Legleiter, C. J., Roberts, D. A., & Lawrence, R. L. (2009). Spectrally based

920 remote sensing of river bathymetry. *Earth Surface Processes and*
921 *Landforms*, 34(8), 1039–1059. <https://doi.org/10.1002/esp.1787>

922 Lillesand, T. M., Kiefer, R. W., & Chipman, J. W. (2015). *Remote Sensing*
923 *& Image Interpretation* (7th ed.). John Wiley & Sons.

924 Lin, Y., Hyyppä, J., & Jaakkola, A. (2011). Mini-UAV-borne LIDAR for fine-
925 scale mapping. *IEEE Geoscience and Remote Sensing Letters*, 8(3),
926 426–430. <https://doi.org/10.1109/LGRS.2010.2079913>

927 Llena, M., Smith, M. W., Wheaton, J. M., & Vericat, D. (2020).
928 Geomorphic process signatures reshaping sub-humid Mediterranean
929 badlands: 2. Application to 5-year dataset. *Earth Surface Processes*
930 *and Landforms*, 45, 1292–1310. <https://doi.org/10.1002/esp.4822>

931 Mandlbürger, G., Pfennigbauer, M., Schwarz, R., Flöry, S., & Nussbaumer,
932 L. (2020). Concept and performance evaluation of a Novel UAV-Borne
933 Topo-Bathymetric LiDAR sensor. *Remote Sensing*, 12(6).
934 <https://doi.org/10.3390/rs12060986>

935 Marteau, B., Vericat, D., Gibbins, C., Batalla, R. J., & Green, D. R. (2017).
936 Application of Structure-from-Motion photogrammetry to river
937 restoration. *Earth Surface Processes and Landforms*, 42(3), 503–515.
938 <https://doi.org/10.1002/esp.4086>

939 Mayr, A., Bremer, M., Rutzinger, M., & Geitner, C. (2019). UNMANNED
940 AERIAL VEHICLE LASER SCANNING for EROSION MONITORING in
941 ALPINE GRASSLAND. *ISPRS Annals of the Photogrammetry, Remote*
942 *Sensing and Spatial Information Sciences*, 4(2/W5), 405–412.
943 <https://doi.org/10.5194/isprs-annals-IV-2-W5-405-2019>

944 Overstreet, B. T., & Legleiter, C. J. (2017). Removing sun glint from
945 optical remote sensing images of shallow rivers. *Earth Surface*
946 *Processes and Landforms*, 42(2), 318–333.
947 <https://doi.org/10.1002/esp.4063>

948 Pearson, E., Smith, M. W., Klaar, M. J., & Brown, L. E. (2017). Can high
949 resolution 3D topographic surveys provide reliable grain size
950 estimates in gravel bed rivers? *Geomorphology*, 293(May), 143–155.
951 <https://doi.org/10.1016/j.geomorph.2017.05.015>

952 Pereira, L. G., Fernandez, P., Mourato, S., Matos, J., Mayer, C., &
953 Marques, F. (2021). Quality control of outsourced LiDAR data acquired
954 with a UAV: A case study. *Remote Sensing*, 13(3), 1–12.
955 <https://doi.org/10.3390/rs13030419>

956 Piégay, H., Arnaud, F., Belletti, B., Bertrand, M., Bizzi, S., Carbonneau,
957 P., Dufour, S., Liébault, F., Ruiz-Villanueva, V., & Slater, L. (2020).
958 Remotely sensed rivers in the Anthropocene: state of the art and
959 prospects. *Earth Surface Processes and Landforms*, 45(1), 157–188.
960 <https://doi.org/10.1002/esp.4787>

961 R Core Team. (2021). *R: A Language and Environment for Statistical*
962 *Computing*. <https://www.r-project.org/>

963 Raj, T., Hashim, F. H., Huddin, A. B., Ibrahim, M. F., & Hussain, A.
964 (2020). A survey on LiDAR scanning mechanisms. *Electronics*
965 *(Switzerland)*, 9(5). <https://doi.org/10.3390/electronics9050741>

966 rapidlasso GmbH. (2021). *LAStools - efficient LiDAR processing software*.

967 <http://rapidlasso.com/LAStools>

968 Reid, H. E., Williams, R. D., Brierley, G. J., Coleman, S. E., Lamb, R.,
969 Rennie, C. D., & Tancock, M. J. (2019). Geomorphological
970 effectiveness of floods to rework gravel bars: Insight from hyperscale
971 topography and hydraulic modelling. *Earth Surface Processes and*
972 *Landforms*, 44(2), 595–613. <https://doi.org/10.1002/esp.4521>

973 Resop, J. P., Lehmann, L., & Cully Hession, W. (2019). Drone laser
974 scanning for modeling riverscape topography and vegetation:
975 Comparison with traditional aerial lidar. *Drones*, 3(2), 1–15.
976 <https://doi.org/10.3390/drones3020035>

977 Resop, J. P., Lehmann, L., & Hession, W. C. (2021). Quantifying the
978 spatial variability of annual and seasonal changes in riverscape
979 vegetation using drone laser scanning. *Drones*, 5(3).
980 <https://doi.org/10.3390/drones5030091>

981 Roussel, J.-R., & Auty, D. (n.d.). *Airborne LiDAR Data Manipulation and*
982 *Visualization for Forestry Applications*. [https://cran.r-](https://cran.r-project.org/package=lidR)
983 [project.org/package=lidR](https://cran.r-project.org/package=lidR)

984 Roussel, J. R., Auty, D., Coops, N. C., Tompalski, P., Goodbody, T. R. H.,
985 Meador, A. S., Bourdon, J. F., de Boissieu, F., & Achim, A. (2020).
986 lidR: An R package for analysis of Airborne Laser Scanning (ALS)
987 data. *Remote Sensing of Environment*, 251(February), 112061.
988 <https://doi.org/10.1016/j.rse.2020.112061>

989 Smith, M. W., Carrivick, J. L., & Quincey, D. J. (2016). Structure from
990 motion photogrammetry in physical geography. *Progress in Physical*
991 *Geography*, 40(2), 247–275.
992 <https://doi.org/10.1177/0309133315615805>

993 Smith, S., Holland, D., & Longley, P. (2003). Investigating the spatial
994 structure of error in digital surface models derived from laser
995 scanning data. *Int. Arch. Photogramm. Remote Sens.*
996 [http://www.isprs.org/proceedings/XXXIV/3-](http://www.isprs.org/proceedings/XXXIV/3-W13/papers/Smith_ALSDD2003.pdf)
997 [W13/papers/Smith_ALSDD2003.pdf](http://www.isprs.org/proceedings/XXXIV/3-W13/papers/Smith_ALSDD2003.pdf)

998 Sofia, G., Fontana, G. D., & Tarolli, P. (2014). High-resolution topography
999 and anthropogenic feature extraction: Testing geomorphometric
1000 parameters in floodplains. *Hydrological Processes*, 28(4), 2046–2061.
1001 <https://doi.org/10.1002/hyp.9727>

1002 Stott, E., Williams, R. D., & Hoey, T. B. (2020). Ground control point
1003 distribution for accurate kilometre-scale topographic mapping using
1004 an rtk-gnss unmanned aerial vehicle and sfm photogrammetry.
1005 *Drones*, 4(3), 1–21. <https://doi.org/10.3390/drones4030055>

1006 Štroner, M., Urban, R., & Línková, L. (2021). A new method for uav lidar
1007 precision testing used for the evaluation of an affordable dji zenmuse
1008 l1 scanner. *Remote Sensing*, 13(23), 1–17.
1009 <https://doi.org/10.3390/rs13234811>

1010 Tarolli, P., & Mudd, S. M. (2020). Introduction to remote sensing of
1011 geomorphology. *Developments in Earth Surface Processes*, 23, xiii–
1012 xv. <https://doi.org/10.1016/B978-0-444-64177-9.09992-6>

1013 Tomsett, C., & Leyland, J. (2019). Remote sensing of river corridors: A

1014 review of current trends and future directions. *River Research and*
1015 *Applications*, 35(7), 779–803. <https://doi.org/10.1002/rra.3479>

1016 Velodyne LiDAR. (2022). *Velodyne Lidar- HDL32E High Resolution Real-*
1017 *Time 3D LiDAR Sensor*. <https://velodynelidar.com/products/hdl-32e/>

1018 Vericat, D., Brasington, J., Wheaton, J. M., & Cowie, M. (2008). Accuracy
1019 assessment of aerial photographs acquired using lighter-than-air
1020 blimps: low-cost tools for mapping river corridors. *River Research and*
1021 *Applications*, 25, 985–1000. <https://doi.org/10.1002/rra.1198>

1022 Wackrow, R., & Chandler, J. H. (2011). Minimising systematic error
1023 surfaces in digital elevation models using oblique convergent imagery.
1024 *Photogrammetric Record*, 26(133), 16–31.
1025 <https://doi.org/10.1111/j.1477-9730.2011.00623.x>

1026 Wallace, L., Lucieer, A., Watson, C., & Turner, D. (2012). Development of
1027 a UAV-LiDAR system with application to forest inventory. *Remote*
1028 *Sensing*, 4(6), 1519–1543. <https://doi.org/10.3390/rs4061519>

1029 Wheaton, J. M., Brasington, J., Darby, S. E., Kasprak, A., Sear, D., &
1030 Vericat, D. (2013). Morphodynamic signatures of braiding
1031 mechanisms as expressed through change in sediment storage in a
1032 gravel-bed river. *Journal of Geophysical Research: Earth Surface*,
1033 118(2), 759–779. <https://doi.org/10.1002/jgrf.20060>

1034 Wheaton, J. M., Brasington, J., Darby, S. E., & Sear, D. A. (2010).
1035 Accounting for uncertainty in DEMs from repeat topographic surveys:
1036 Improved sediment budgets. *Earth Surface Processes and Landforms*,
1037 35(2), 136–156. <https://doi.org/10.1002/esp.1886>

1038 Williams, R. D., Bangen, S., Gillies, E., Kramer, N., Moir, H., & Wheaton,
1039 J. (2020b). Let the river erode! Enabling lateral migration increases
1040 geomorphic unit diversity. *Science of the Total Environment*, 715,
1041 136817. <https://doi.org/10.1016/j.scitotenv.2020.136817>

1042 Williams, R. D., Brasington, J., Vericat, D., & Hicks, D. M. (2014).
1043 Hyperscale terrain modelling of braided rivers: Fusing mobile
1044 terrestrial laser scanning and optical bathymetric mapping. *Earth*
1045 *Surface Processes and Landforms*, 39(2), 167–183.
1046 <https://doi.org/10.1002/esp.3437>

1047 Williams, R. D., Lamy, M. Lou, Maniatis, G., & Stott, E. (2020a). Three-
1048 dimensional reconstruction of fluvial surface sedimentology and
1049 topography using personal mobile laser scanning. *Earth Surface*
1050 *Processes and Landforms*, 45(1), 251–261.
1051 <https://doi.org/10.1002/esp.4747>

1052 Woodget, A. S., Carbonneau, P. E., Visser, F., & Maddock, I. P. (2015).
1053 Quantifying submerged fluvial topography using hyperspatial
1054 resolution UAS imagery and structure from motion photogrammetry.
1055 *Earth Surface Processes and Landforms*, 40(1), 47–64.
1056 <https://doi.org/10.1002/esp.3613>

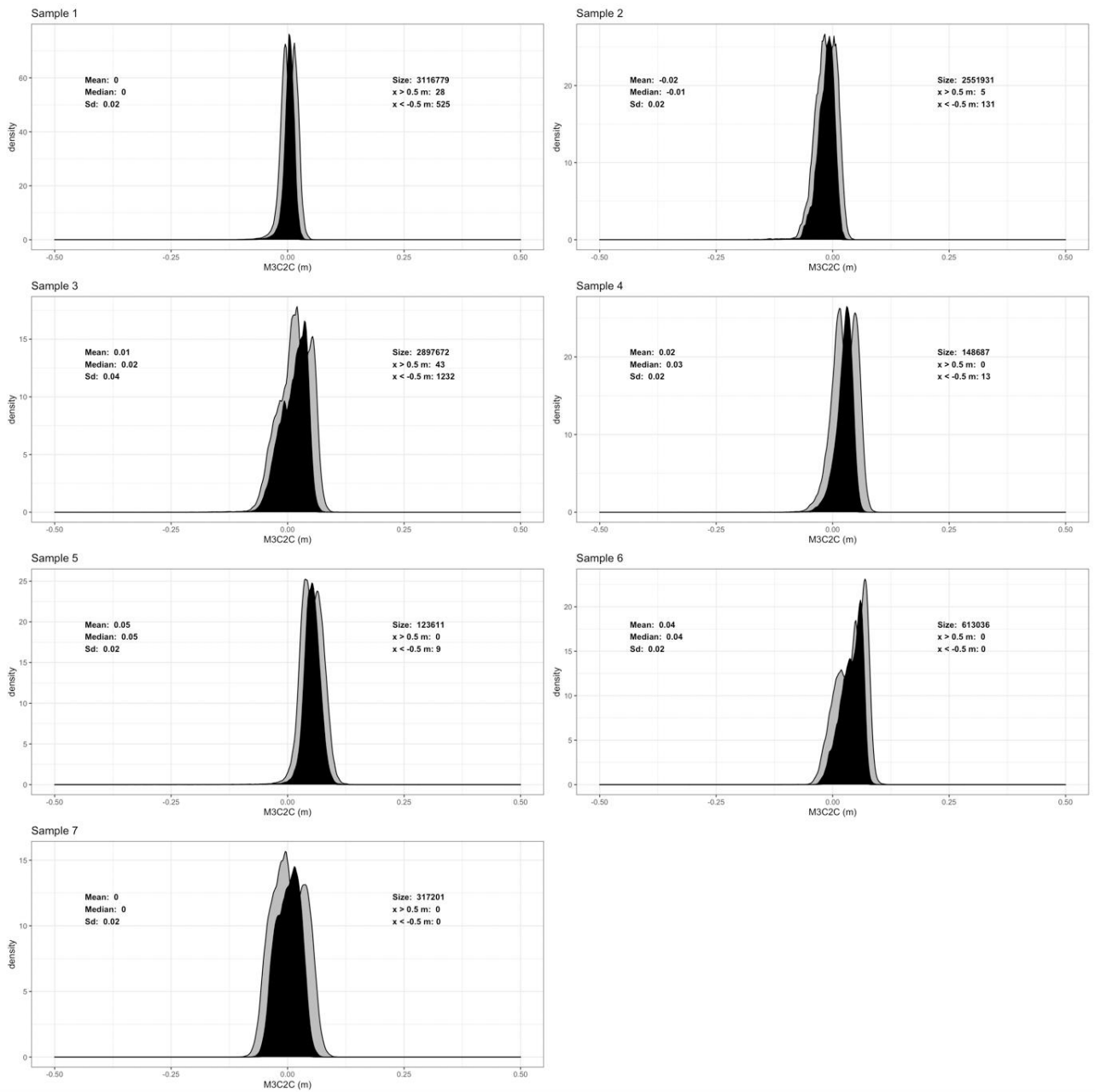
1057 Woodget, A. S., Dietrich, J. T., & Wilson, R. T. (2019). Quantifying below-
1058 water fluvial geomorphic change: The implications of refraction
1059 correction, water surface elevations, and spatially variable error.
1060 *Remote Sensing*, 11(20), 1–33. <https://doi.org/10.3390/rs11202415>

1061 Zhang, K., Chen, S. C., Whitman, D., Shyu, M. L., Yan, J., & Zhang, C.
1062 (2003). A progressive morphological filter for removing nonground
1063 measurements from airborne LIDAR data. *IEEE Transactions on*
1064 *Geoscience and Remote Sensing*, 41(4 PART I), 872–882.
1065 <https://doi.org/10.1109/TGRS.2003.810682>
1066 Zhang, W., Qi, J., Wan, P., Wang, H., Xie, D., Wang, X., & Yan, G.
1067 (2016). An easy-to-use airborne LiDAR data filtering method based on
1068 cloth simulation. *Remote Sensing*, 8(6), 1–22.
1069 <https://doi.org/10.3390/rs8060501>
1070

- 1 **Supplementary Material A: RTK-GNSS measurement quality**
- 2 Table S1: Coordinate quality (CQ) and occupation details of the RTK-GNSS
- 3 measurements used for comparison to UAV LiDAR data.

Field site	GNSS Point Type	Occupation Time	Coordinate Quality Type	Mean (m)	Standard Deviation (m)
Garscube	Ground Control Targets	30 s	Horizontal (2D) CQ	0.005	0.001
			Vertical (1D) CQ	0.008	0.002
	Football Pitch markings	5 s	Horizontal (2D) CQ	0.008	0.002
			Vertical (1D) CQ	0.012	0.003
Feshie	Ground Control Targets	1 min	Horizontal (2D) CQ	0.004	0.001
			Vertical (1D) CQ	0.006	0.002
	Road Orthometric Height	5 s	Horizontal (2D) CQ	0.009	0.005
			Vertical (1D) CQ	0.014	0.007
	River Gravel Orthometric Height	5 s	Horizontal (2D) CQ	0.006	0.002
			Vertical (1D) CQ	0.011	0.002
	TLS Targets	Minimum 5 mins	Horizontal (2D) CQ	0.0002	0.0001
			Vertical (1D) CQ	0.0006	0.0004
	Vegetation Orthometric Height	1s	Horizontal (2D) CQ	0.007	0.012
			Vertical (1D) CQ	0.004	0.008

5 **Supplementary Material B: Distribution of M3C2 differences**
 6 **(individual sub-areas)**



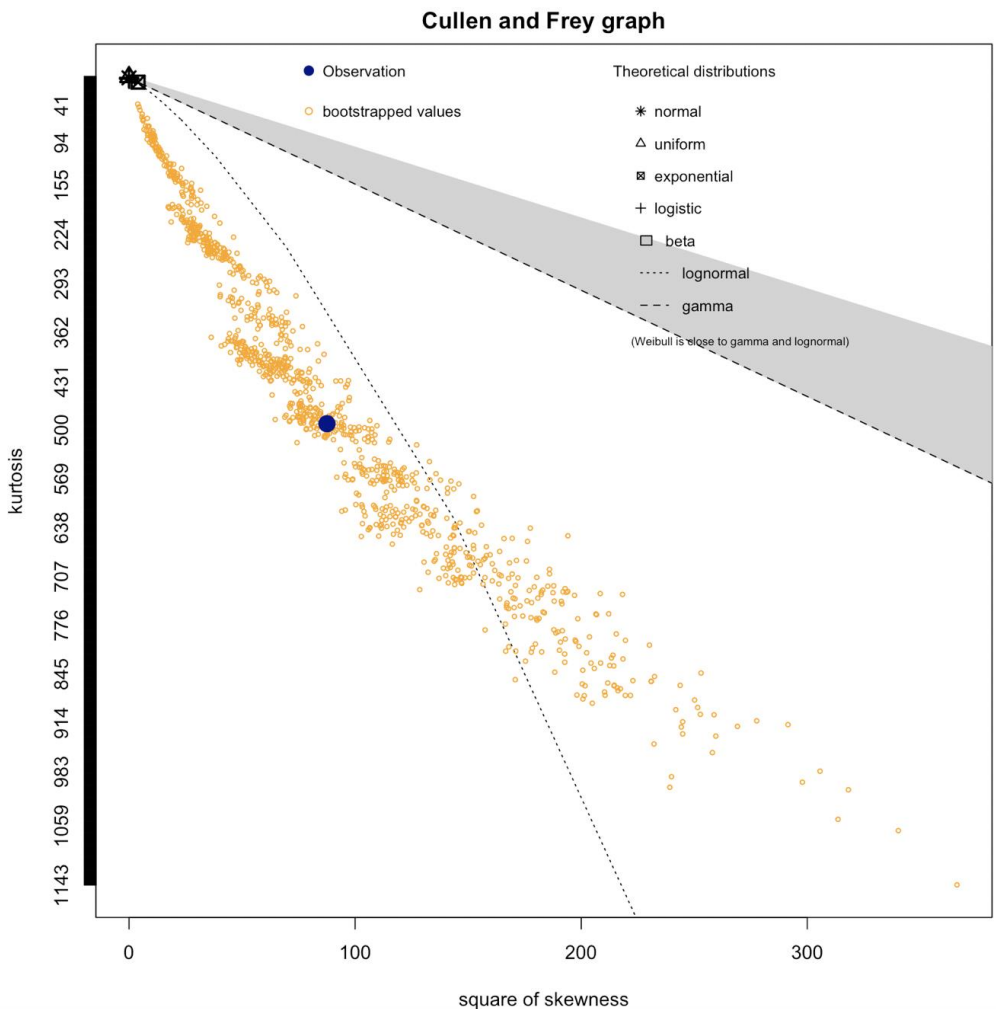
7

8 Figure S1: The distribution of the sampled M3C2 differences (Samples 1-
 9 7) between the UAV-LiDAR and the TLS point clouds (River Feshie, black).

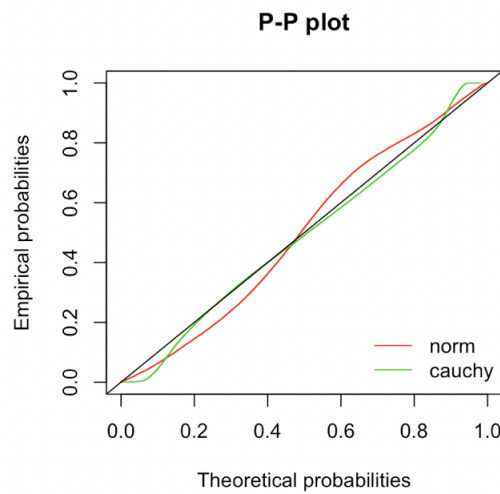
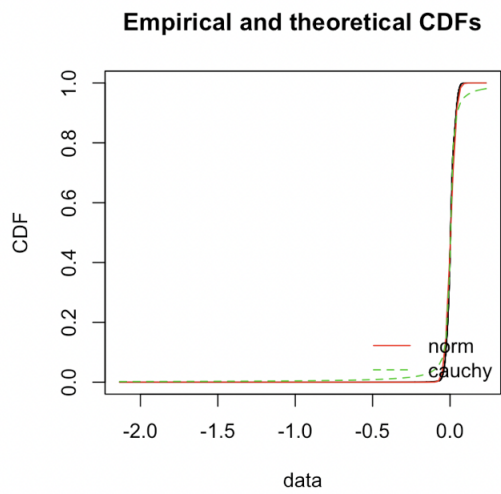
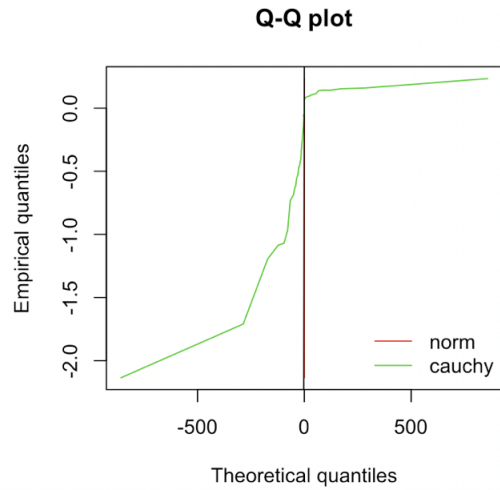
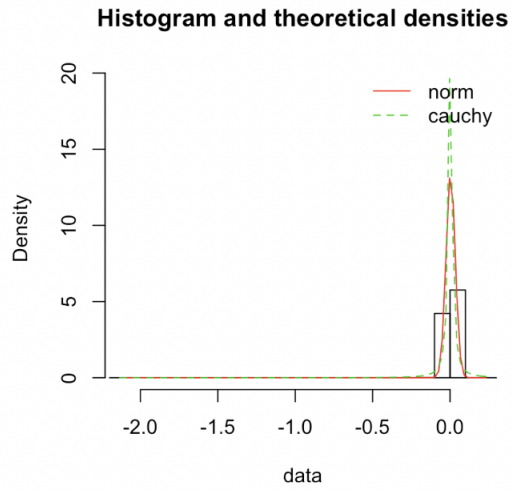
10 The grey histograms demonstrate the maximum and the minimum
 11 expected distributions (M3C2-uncertainty and M3C2+uncertainty for left
 12 and right respectively).

13 **Supplementary Material C: Distribution fitting for the combined**
14 **M3C2 sample (River Feshie).**

15 Figure S2 shows the Cullen and Frey diagram for the identification of
16 candidate distributions for the combined M3C2 sample. The bootstrapped
17 samples fall in the "symmetric" region, and we test the normal and the
18 Cauchy distributions, as the histogram indicates a mean and a median
19 approximating 0. The normal distribution outperforms the Cauchy at the
20 tails of the distributions (Q-Q plot, Figure S3). However, the Cauchy
21 distribution outperforms the normal in terms of central tendency (P-P plot,
22 Figure S3). The histogram and CDF diagrams lead to the same conclusions.
23 The confirmation for the selection of the distribution comes from the
24 goodness of fit criteria (Table S2) where the selected distribution (Cauchy)
25 marginally outperforms the normal for both the Akaike's and the Bayesian
26 calculation.



27
28 Figure S2: Cullen and Frey diagnostics for the combined M3C2 sample.
29 The area variation of bootstrapped values (yellow) indicates that the best
30 candidate distributions less likely to be non-symmetric. This is supported
31 graphically by the form of the histogram (Figure S3).



32

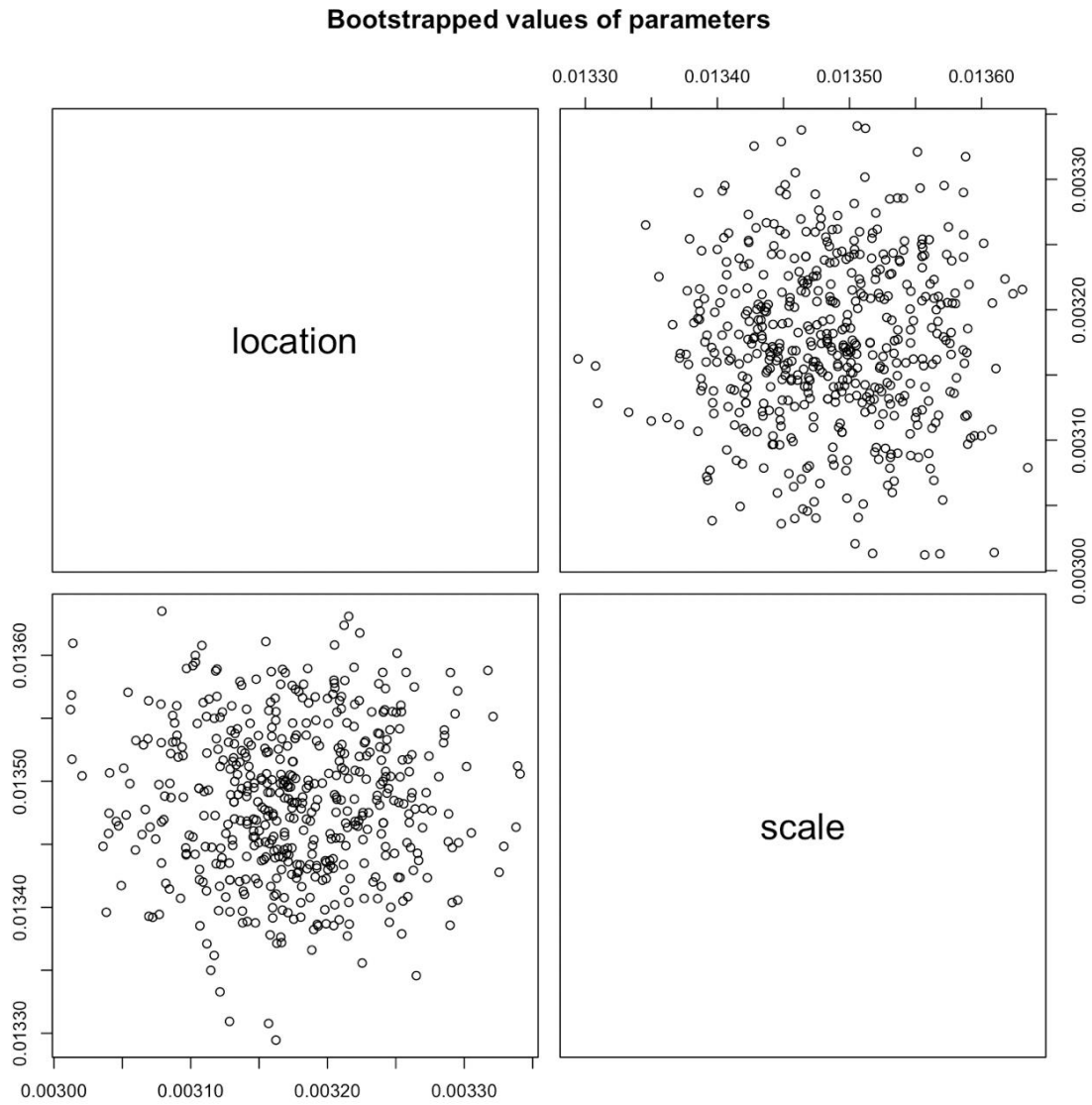
33 Figure S3: Fitting plots for the examined normal and Cauchy distributions.

34 Table S2: Goodness of fit statistics for the tested normal and Cauchy
 35 distributions. The Cauchy distribution outperforms the normal (marginally)
 36 as both the Akaike's and the Bayesian criteria are smaller.

Goodness-of-fit statistics		
	Normal	Cauchy
Kolmogorov-Smirnov statistic	0.06752856	0.06044401
Cramer-von Mises statistic	186.06562228	60.54967189
Anderson-Darling statistic	Inf	851.88017587
Goodness-of-fit criteria		
	Normal	Cauchy
Akaike's Information Criterion	-420356.9	-425859.6
Bayesian Information Criterion	-420337.8	-425840.6

37

38 Figure S4 demonstrates the stability of the selected distribution for M3C2
 39 combined sample. For the Cauchy distribution 1000 bootstrapped
 40 parameters were cross compared, revealing a variation of approximately
 41 0.003 for the location parameter and 0.013 for the scale parameter. This
 42 range is also confirmed in Table S3, where 97.5% of the bootstrapped
 43 parameters fall within those ranges. The differences are marginal,
 44 indicating good stability of the selected distribution for the scaling of the
 45 data.



46

Figure S4: Bootstrap parameters for selected distributions.

47

48 Table S3: Statistics of the bootstrapped distribution parameters (Cauchy).

	Median	2.5%	97.5%
Location	0.003171376	0.003050031	0.00329234
Scale	0.013484919	0.013376707	0.01359002

49

50